The Effect of Helium and Scandium Ion Implantation on the Structural, Vibrational and Piezoelectric Properties of Aluminium Nitride Thin Films

by

Vaibhav Sharma

A thesis submitted to the Victoria University of Wellington in partial fulfilment of the requirements for the degree of Master of Science in Physics.

Victoria University of Wellington
2019

Abstract

Aluminium nitride (AlN) is one of the leading piezoelectric materials for commercial bulk acoustic wave devices due to its useful properties such as moderate piezoelectricity, high acoustic velocities and low thermal drift. In this thesis, possibilities of strain generation or alloy formation in AlN thin films are investigated with the aim to further increase the piezoelectric response. To this end, helium and scandium ions are implanted in the AlN films at different concentrations. The changes in the vibrational, structural and piezoelectric properties of the AlN thin films from the implantation are investigated using experimental techniques such as Raman spectroscopy, X-ray diffraction (XRD) and piezoelectric force microscopy (PFM).

This study demonstrates that the ion beam implantation technique is well-suited to generate uniaxial strain along the c-axis, without modifying the strain in the a-axis basal-plane. We measure a strain increase of 1% for He and Sc at the highest fluence of 1 x 10^{17} ions/cm^2. Interestingly, for both implantations, we observe a secondary phase created at fluences above 1 x 10^{16} ions/cm^2 and above, which could mark an amorphization threshold. A possible interpretation is that for the He implantation, the secondary phase is from the formation of He bubbles in the lattice. For the case of Sc implantation this phase could be from formation of nano-crystalline Sc in the first few nanometres of the film or ScAlN alloying effects.

We did not find evidence of an increase in the piezoelectric response for the He implantation. XRD scans revealed the implantation of He into the films generated uniaxial strain along the c-axis, with a simultaneous reduction in piezoelectric response as measured by PFM. The reduction in piezoelectricity is attributed to introduction of disorder in the lattice as confirmed by Raman spectroscopy. For the Sc implantation, a reduction in the measured amplitude from PFM for fluences of 1 x 10^{15} ions/cm^2 and 5 x 10^{15} ions/cm^2 is also attributed to disorder introduced by the implantation. We find that at a fluence of 1 x 10^{16} ions/cm^2, the film has similar electromechanical responses as un-implanted which makes an interesting case to investigate its piezoelectric properties at higher fluences and after annealing.

Acknowledgements

The universe is full of questions,

Star (2001) ponders, *"Is mayonnaise an instrument?"*

Table of Contents

Chapter 1 Introduction

1.1 Motivation and Context of Work

Wireless communication is of ever-increasing importance to our everyday lives. We utilise the internet more heavily now than ever before for video streaming, file sharing, e-banking, e-learning to name a few. The next generation of cellular technology, known commonly as "5G" promises to be a revolution in the way we utilise wireless communication. It proposes data transfer speeds of $1 - 10$ Gb/s and round-trip latencies of $1 - 5$ ms, each an order of magnitude faster than 4G [1, 2]. Furthermore, 5G will allow for up to 100x more devices to be connected to the network than currently possible in 4G [1, 2]. This should greatly help in the implementation and standardisation of modern and near-future applications such as self-driving cars and enhanced virtual reality which require extremely low latency (< 5 ms) and fast download/upload speeds with high reliability.
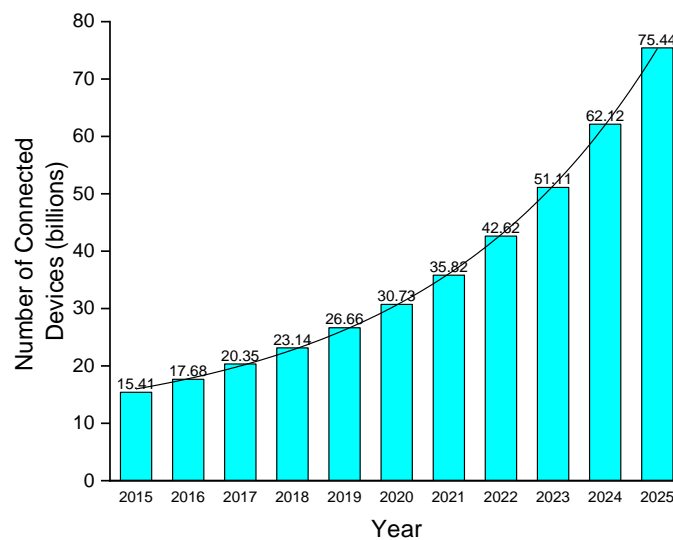
Figure 1: number of connected devices (billions) in the past and forecasted for the near-future (source: IHS [3]).

Societal usage of the internet is increasing at an exponential rate [2]. In the previous decade the amount of intellectual property data handled by wireless networks has increased a hundredfold, from 3 exabytes in 2010 to 180 exabytes in 2018, predicted to increase to 500 exabytes in 2020 [2]. Similarly, the number of connected devices is increasing exponentially, as shown in Figure 1 [3]. The current long-term evolution (LTE) strategy for 4G has been fully

deployed and reached maturity [2]. 4G utilises the electromagnetic (EM) spectrum between 0.5 - 6 GHz. Unfortunately, this spectrum is very crowded with applications and is almost fully utilised. Only incremental increases in bandwidth allocation are possible from the advancements in radio-filter technology. One way is to reduce the amount of "wasted spectrum" between bandwidths by increasing the quality factors of filters (see section 1.2), which will not meet the requirements of the next decade [1, 2]. What was sufficient yesterday may not be tomorrow. 5G aims to alleviate these issues by "opening up" very high carrier frequency ranges between 3 GHz – 300 GHz [1, 2, 4].

Naturally, the development and implementation of innovative technology will host new challenges and require novel solutions. To move to frequencies upwards of 300 GHz, significant advances must be made to radio-frequency (RF) filter technology. The search for filters with low thermal drift, high efficiency and low power consumption is driving industry to develop piezoelectric materials to make this possible.

1.2 Acoustic Filters

Wireless devices communicate via electromagnetic (EM) waves. For each application in a device, a specific frequency range is prescribed. For example, WiFi is utilised in 2 bands. The lower frequency 2 GHz band allocates bandwidth in the range 2400 and 2500 MHz whereas the higher frequency 5 GHz is between 5725 and 5875 MHz [5]. Band-pass filters process EM waves and allow a desired bandwidth to be transmitted while heavily attenuating all other frequencies. These are known as radio-frequency (RF) or acoustic filters.

Modern smartphones now contain more than 60 RF-filters for various applications and signal processing [4]. At the 1 GHz frequency range, the wavelength is on the order of tens of cm – far too big for cavity or waveguide filters. In order to filter these signals, the EM wave is coupled into an acoustic wave in a piezoelectric material where the acoustic velocity is typically of the order of 1,000 – 10,000 m/s, about 5 orders of magnitude lower than EM waves, causing the wavelength to drop by the same order [4, 6, 7].

A noisy incident EM wave may have a range of frequencies and amplitudes. An acoustic filter will select out a narrow bandwidth from the input signal, as shown in Figure 2. This is determined by the characteristic frequency and mechanical Q factor of the filter,

$$Q = \frac{f_c}{\Delta f} \qquad\qquad (1)$$

where f_c is the characteristic or central frequency and Δf is the bandwidth [4]. Frequencies outside of the desired range are heavily attenuated.
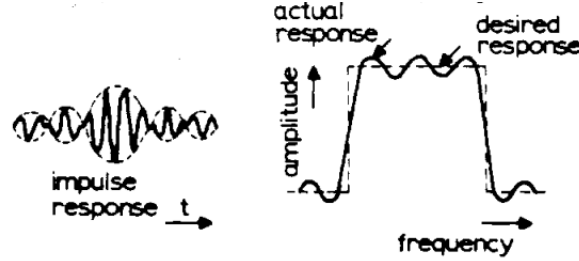
Figure 2: typical frequency response for a band-pass filter from [8].

Acoustic RF filters come in two types: surface acoustic wave (SAW) and bulk acoustic wave (BAW) of which BAW has sub-types of film bulk acoustic resonators (FBARs) and solidly mounted resonators (SMRs). A basic schematic of each is presented in Figure 3.
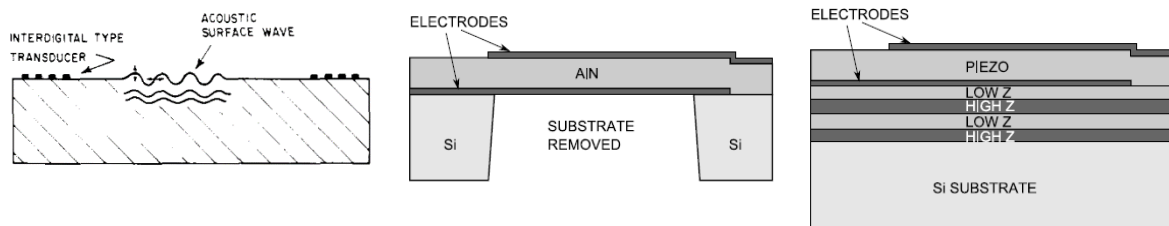
Figure 3: Side-on views of SAW (left) [7], FBAR (middle) [6] and SMR (right) [6].

Although similar in operating physics, SAWs and BAWs differ in the way the acoustic wave is generated, making them suitable for different applications.

In a SAW device, periodically placed interdigital transducers (IDT) serve as electrodes to generate an acoustic wave which propagates along the *surface*. The wavelength of the wave is determined by the IDT spacing and the velocity of the material in the direction of propagation. The central frequency is given by [9],

$$f_c = \frac{v_s}{\Delta x} \tag{2}$$

where v_s is the Rayleigh velocity and Δx is twice the distance between adjacent fingers in the IDT.

In BAW devices, a standing wave is made between the top and bottom electrodes inside which the piezoelectric material is wedged (AlN material in the middle case presented in Figure 3). The central frequency is given by [9],

$$f_n = \frac{n}{2l} v_l \tag{3}$$

where n is a positive integer that denotes the resonance mode, l is the length between the top and bottom electrode and v_l is the intrinsic longitudinal acoustic velocity of the material, typically of the order of 1,000 – 10,000 m/s. SMRs operate in a similar way to FBARs except they use alternating low impedance, high impedance Bragg reflectors (denoted low and high Z in Figure 3) to reflect the acoustic wave back into the piezoelectric material to reduce loss [6]. FBARs use a free-standing structure with the impedance mismatch due to air.

Due to the low cost of manufacture of SAW devices, they form a dominant part of the mobile device market for filters below 2 GHz. However, due to parasitic losses the Q factor of SAW devices remains below 1000, making it problematic for use at higher frequencies, where it is more economical and practical to use BAW [4, 6]. Moreover, the physical thickness of BAW is inversely proportional to the frequency at which it resonates, allowing for extreme miniaturisation at high frequencies to be used in small devices. Overall, at the high frequency end (> 2GHz) BAW devices provide better Q factor, thermal stability and power handling capabilities than SAW [6]. Additionally, at frequencies higher than what is currently used (> 6GHz), the thickness of the Bragg reflectors in SMRs may be reduced to an unrealistic value, making it more desirable to use FBARs.

1.2.1 Piezoelectric Materials

As mentioned before, piezoelectric materials allow for the conversion of electrical energy to mechanical energy in acoustic filters. They are the basis upon which RF filters function. The origin of piezoelectricity in materials and its relationship with useful parameters such as the electromechanical coupling coefficient (K^2) and phase velocity are discussed in more detail in section 2.2.1.

AlN is the dominant piezoelectric material used in commercial FBARs. Although it has a moderate piezoelectric charge coefficient d_{33} of 5.1 pm/V, it combines a low thermal drift (-25 ppm/°C) with high acoustic speeds (longitudinal phase velocity of 11,250 m/s) [6, 10, 11].

Useful properties of AlN are summarised in Table 1 in section 2.2. These properties are among the best in the group III nitrides, which is why AlN is attractive [10]. Typical FBARs made of AlN have K^2 (ratio of transmitted energy to applied energy) of about 6.5 % [6, 12]. It is also complementary metal-oxide-semiconductor (CMOS) compatible which eases fabrication processes [6, 10].

ZnO is another common piezoelectric material used in SAW. It has better piezoelectric properties than AlN, allowing typical K^2 of 9.2%. However, due to its relatively large thermal drift (-60 ppm/^{o}C) and low acoustic velocities it is better suited for lower frequency, less-demanding applications [6].

1.3 Research Interest

A desirable approach for improving the functionality of acoustic filters is to increase the electromechanical coupling coefficient (K^2) as this will allow for more efficient coupling between the applied electrical energy and stored mechanical energy, which will boost its performance at higher frequencies. One way to do this is to increase the piezoelectric charge coefficient (d_{33}) of the material as K^2 is proportional to d_{33}^2 [12]. A more detailed description of these parameters are written in section 2.2.1.

Our hypothesis is that the technique of ion beam implantation can be used to introduce strain or form alloying that will result in an increase in the piezoelectric charge coefficient d_{33} of AlN thin films. It has been previously reported that a d_{33} increase of 500% is achievable in $Sc_xAl_{1-x}N$ alloy thin films grown carefully using a dual co-sputtering method [10]. Using this framework, we will implant scandium (Sc^+) ions into AlN thin films at various concentrations and investigate its effects on its vibrational, structural and piezoelectric properties. To do so, we shall characterise the films using Raman spectroscopy, X-ray diffraction (XRD), piezoelectric force microscopy (PFM) and more.

We will start this study with implanting the AlN films with helium (He^+) ions. It has been reported that He ion implantation can create uniaxial strain in SnO_2 films that has been shown to reduce the band gap in a continuous relationship [13]. The strain induced may make the material more non-centrosymmetric that could increase its piezoelectricity. Next, we will move on to AlN implanted with Sc that could strain the c-axis in a similar way as He. The Sc may also bond with the N to form ScN that could potentially result in it being easier for the N to oscillate along the c-axis, thereby increasing the piezoelectric response.

The overall aim of this study is to gain a better understanding of the ion implantation process in AlN thin films and its effects on the structural, vibrational and piezoelectric properties. In particular, the desire is to improve the piezoelectric properties by increasing the piezoelectric charge coefficient d_{33} as it may present a step forward in the next generation of RF filters. Figure 4 illustrates the basic premise behind ion implantation into the piezoelectric material of an existing FBAR device for easy modification.
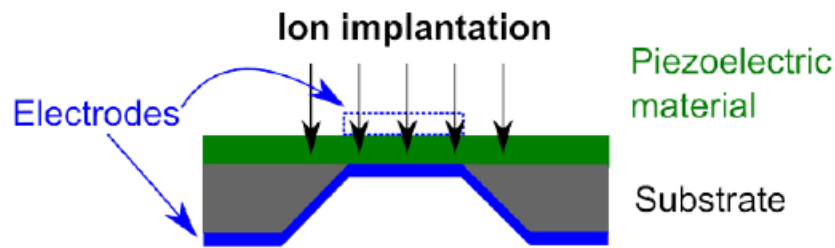
Figure 4: FBAR showing modification of piezolayer prior to top electrode deposition.

To the best of our knowledge, analysis on the effects of ion beam implantation on the acoustic properties of filters has not been done before so information on these aspects may be useful to the RF filter industry.

1.4   Thesis Framework

Chapter 2 shall provide the scientific background important to this project.

- Literature review of selected scientific articles for the two approaches
- Description of AlN crystal structure and properties
- Implantation procedure and basic physics; thin film details
- Background information of experimental methods for Raman spectroscopy, X-ray diffraction, atomic force microscopy and piezoelectric force microscopy

Chapter 3 will present the experimental results and simulations for AlN implanted with He.

- Dynamic Transport and Range of Ions in Matter (DTRIM) simulations
- Raman spectroscopy
- X-ray diffraction
- Piezoelectric force microscopy
- Conclusions

Chapter 4 will present the DTRIM simulations and experimental results for AlN implanted with Sc. These will be the same as above for He, plus Rutherford Backscattering (RBS) and current-voltage characterisation.

Finally, chapter 5 will summarise the project and its outcomes and provide recommendations for future work.

Chapter 2 Scientific Background

2.1 Literature Review

We shall now review the literature that formed the basis of this project. Our hypothesis is that ion beam implantation techniques can be used to increase the d_{33} in AlN thin films. Firstly, we shall discuss the AlN implanted with He, followed by Sc.

2.1.1 He Implantation (light ion)

Lorenz *et al.* recently reported the *c*-axis (vertical) is over 4 times more susceptible to changes than the *a*-axis (horizontal) from ion implantation in *wurtzite*-GaN thin films [14]. This could allow for interesting strain-engineering along the *c*-axis which can be easily modified, with little change to the *a*-axis. Herklotz *et al.* were able to produce uniaxial stain along the *c*-axis in SnO$_2$ films via the implantation of He, as illustrated in Figure 5. This gas is inert and so can not chemically react with the target, rather it came to rest in interstitial sites that expanded the *c*-axis while the *a*-axis was unperturbed [13].
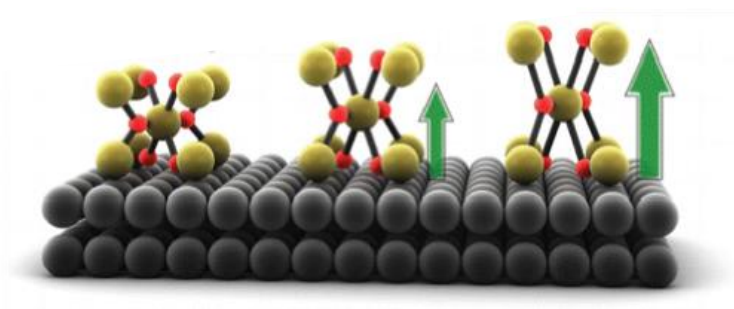
Figure 5: Uniaxial strain (tensile) in SnO$_2$ [13].

The idea is to combine the aspects of these two papers and apply it to *c*-axis oriented *wurtzite*-AlN thin films. We aim to produce uniaxial strain in our films via the implantation of He that would change the elastic properties of the lattice in the *c*-axis and make the unit cell more non-centrosymmetric, to see if this would increase the piezoelectric charge coefficient (d_{33}) of AlN.

2.1.2 Sc Implantation (heavy ion)

In 2009, Akiyama *et al.* reported an increase in d_{33} for $Sc_xAl_{1-x}N$ alloy thin films with increasing Sc concentration with a maximum of 27.6 pm/V for *x = 0.43*, more than 500 % greater than pure AlN (5.1 pm/V) (see Figure 6) [11, 15]. This was the highest recorded piezoelectric charge coefficient among the tetrahedrally bonded semiconductors. The $Sc_xAl_{1-x}N$ thin films (of thickness 0.5 – 1.1 µm) were grown under controlled conditions using dual co-sputtering techniques. More details of the growth and preparation of the films can be found in [10, 15].
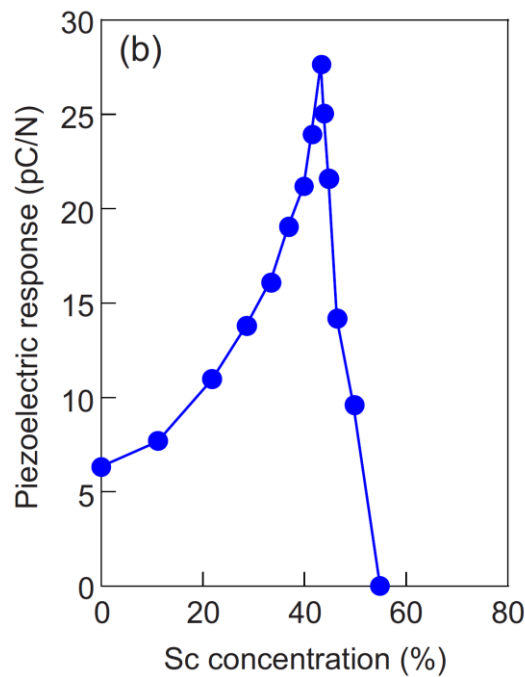
Figure 6: dependence of piezoelectric charge coefficient d_{33} of $Sc_xAl_{1-x}N$ alloy thin films on Sc concentration [15].

Shortly after this discovery, Tasnádi *et al.* published a detailed article that explained the origin of this remarkable piezoelectric increase [16]. Using density functional theory and other software designed for such calculations at the quantum level, they showed the increase in d_{33} was due to the softening of the C_{33} elastic stiffness. ScN has a ground state rock-salt structure (cubic) that is non-polar. However, Farrer *et al.* predicted a hexagonal ScN structure that is metastable (non-polar). *hexagonal*-ScN has a *c/a* of 1.27 and nearly fivefold coordination of nitrogen whereas *wurtzite*-AlN has a *c/a* of 1.60 and tetrahedral coordination of nitrogen [16]. The coexistence of these two parent binary phases with different bonding arrangements and

lattice constants create a frustrated system that is highly sensitive to strain, drastically increasing d_{33}; experimentally measured to be maximum for $x = 0.43$ [10, 15].

The piezoelectricity can be discussed for group III-V nitrides using the following relation [16],

$$e_{33}(x) = e_{33}^{\text{clamped-ion}}(x) + \frac{4eZ^*(x)}{\sqrt{3}a(x)^2}\frac{du(x)}{d\delta} \tag{4}$$

the terms a (lattice parameter) and eZ^* (nuclear charge) are properties of the wurtzite cell and are unchanged. e_{33} is a term that describes the piezoelectric response and is proportional to d_{33}. The clamped-ion term represents the electronic response with respect to strain. The $du(x)/d\delta$ term represents the change in internal parameter with respect to strain and increasing this essentially allows the nitrogen to vibrate up and down more easily between the two phases, increasing the piezoelectric charge coefficient.

In summary, $Sc_xAl_{1-x}N$ alloy thin films have been reported to have a significantly larger piezoelectric charge coefficient than pure AlN. It will be interesting to investigate whether doping AlN with Sc via ion implantation techniques will increase the d_{33} through similar mechanisms reported in literature [10, 15]. The theory of ion implantation relevant to this discussion is presented in more detail in section 2.4.

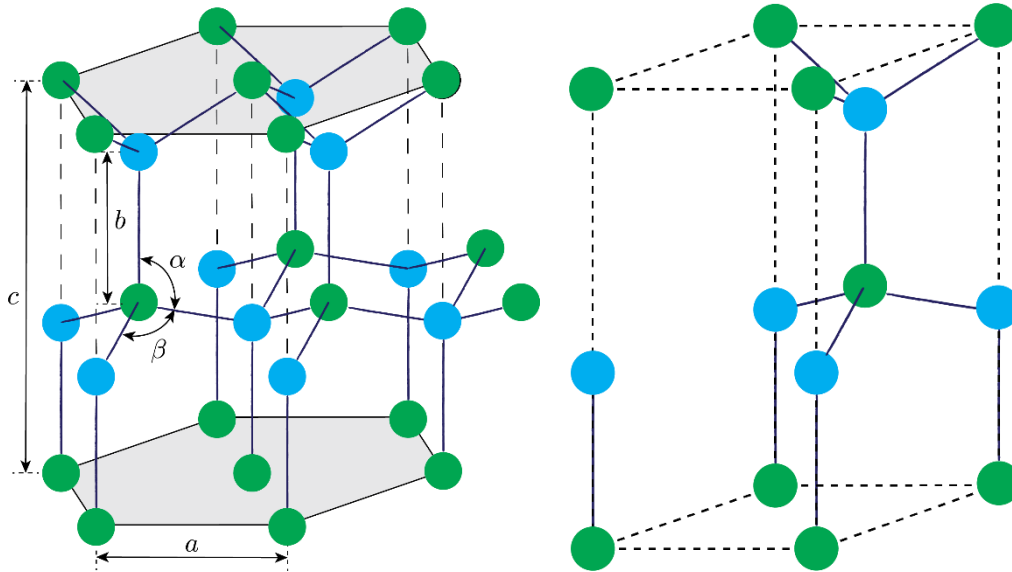## 2.2 Aluminium Nitride: Properties and Structure

Figure 7: crystal structure of AlN; interlocking HCP lattices (left); primitive cell (right). Green and blue circles represent Al and N atoms, respectively. Lattice parameters a and c, bond angles α and β and characterisation length b are labelled. Unit cell on right. Illustration created with aid from [17].

AlN is a group III nitride semi-conductor with a large band gap of 6.2 eV [18]. It has good mechanical strength, corrosion resistance and is compatible with integrated circuit (IC) fabrication processes [6, 19]. Table 1 summarises some important properties of AlN. AlN crystallises in the wurtzite structure, alongside ZnO, InN, GaN. Figure 7 illustrates the wurtzite structure of AlN. This structure consists of two interpenetrating sublattices of Al^+ and N^- ions in a hexagonal close-packed (HCP) arrangement. The two HCP sublattices are bonded together via ionic bonds. Each Al atom is surrounded by 4 N atoms sitting in the corner of a tetrahedron and *vice versa*, meaning AlN lacks inversion symmetry; or is non-centrosymmetric. This property grants piezoelectricity, which will be discussed in section 2.2.1.

The c lattice parameter is 4.98 Å and signifies the height of the unit cell; or the vertical distance between two repeating atoms; hence the z-axis is referred to as the c-axis. The a lattice parameter is the distance between two adjacent atoms in the basal (xy) plane and is 3.11 Å in AlN. Due to hexagonal symmetry, each atom is equidistant to its nearest neighbour in the basal plane. In an ideal wurtzite structure, $c/a = \sqrt{8/3}$. The bond angles α and β are 109.5°. The sublattices are fractionally displaced along the c-axis by the internal parameter u which is 3/8 in an ideal wurtzite, such that $b = uc$. For more information on the wurtzite structure, please refer to [20].

Table 1: summary of important structural and electronic properties of AlN [6, 18]

Property	Value	Units
Band gap	6.2	eV
Density	3.26	g/cm^3
d_{33}	5.1 ± 0.1 [11]	pm/V
K^2	6.5 %	-
Longitudinal wave velocity	11,250	m/s
Shear wave velocity*	6,329	m/s
Lattice parameter: a	3.112	Å
Lattice parameter: c	4.982	Å
Thermal conductivity	320	W/mK
Thermal expansion coefficient	4.6×10^{-6}	K^{-1}
Thermal drift	-25	ppm/K
Melting point	> 2200	K
Relative permittivity	9.66	-
Refractive index	2.15	-
CMOS compatible	Yes	-

2.2.1 Piezoelectricity

Piezoelectricity comes from the Greek word "piezo" meaning pressure, translating to "electricity from pressure" [21]. Indeed, it is the property of a class of materials that become polarised or "generate electricity" when they expand/contract due to stress or pressure [22]. The reverse is also true where a material will expand/contract from the application of an external electric field. This effect was first discovered by Carolus Linnaeus and Franz Aepinus in the middle of the 19th century, however it wasn't until late the 19th century when brothers Jacques and Pierre Curie started investigating that piezoelectricity became a research field in physics [21, 22].
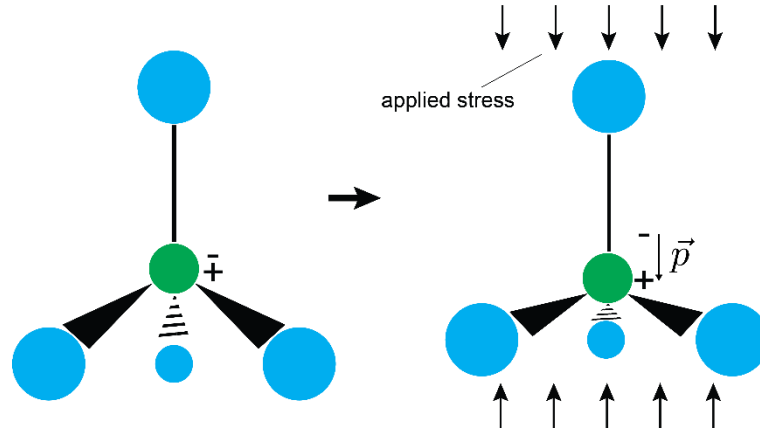
Figure 8: simple illustration of applied stress on aluminium nitride (AlN) inducing an electric dipole $\vec{p}$. Green: Al atom; blue: N atom. Note: this is not the unit cell for AlN, but illustrates the tetrahedral arrangement of N around Al.

Materials that are non-centrosymmetric (or lack inversion symmetry) are piezoelectric. In a centrosymmetric material, if we take the location of an atom in the unit cell (x, y, z) and translate it to (-x, -y, -z) there will be an identical atom at this position for all atoms in the unit cell (the origin in this case is the centre of positive and negative charges, which are at the same position for an unpolarised material). A non-centrosymmetric material lacks this property and will develop a dipole when strained along a polar axis since the centre of positive and negative charges will displace. Piezoelectricity is very common in inorganic materials as 20 out of 32 symmetry groups are piezoelectric [23].

The piezoelectric charge coefficient is commonly used to characterise the amount of expansion per applied voltage, with d_{ij}. This is a 2nd rank tensor with constant values in pm/V. Depending on the material structure it is possible to expand the material in directions other than the direction the electric field is applied. In most cases, the expansion in the *z*-axis caused by an electric field in the *z*-axis is important and is characterised by d_{33}. Furthermore, the electromechanical coupling coefficient K^2 is a particularly useful value that relates the applied electrical energy and stored mechanical energy [12, 20],

$$K^2 = \frac{d_{33}^2}{C_{33}\varepsilon_{33}} = \frac{\text{stored mechanical energy}}{\text{applied electrical energy}} \tag{5}$$

where d_{33} is the piezoelectric charge coefficient, C_{33} the elastic stiffness and ε_{33} the permittivity along the c-axis. Furthermore, using the wave equation for elastic solids and the constitutive relations, it is possible to show that the acoustic velocity in piezoelectric materials is enhanced by a factor of $(1 + K^2)^{\frac{1}{2}}$,

$$v_p = v_p'(1 + K^2)^{\frac{1}{2}} \tag{6}$$

where v_p' is the regular acoustic velocity for the same material if it were non-piezoelectric,

$$v_p' = \left(\frac{C_{33}}{\rho}\right)^{\frac{1}{2}}$$

where ρ is the density [12, 20]. For aluminium nitride with a K^2 of 6.5 % this enhancement is about 3% [6].

2.2.2   X-Ray Diffraction Relationship

The spacing between crystallographic planes (d_{hkl}) in the wurtzite structure can be expressed by the following relation [20],

$$\frac{1}{d_{hkl}^2} = \frac{4}{3}\left(\frac{h^2 + hk + k^2}{a^2}\right) + \frac{l^2}{c^2} \tag{7}$$

where a and c are the standard lattice parameters and h, k and l are Miller indices corresponding to the $\vec{a}, \vec{b}$ and $\vec{c}$ crystallographic vectors, respectively. For wurtzite structures, (001) planes will not produce an XRD peak due to destructive interference. However, peaks corresponding to the (002) and (100) planes are observed. Therefore, it is of value to determine the relation between the a and c lattice parameters to the d spacing of these planes using equation (7),

$$d_{002} = \frac{c}{2} \tag{8}$$

$$d_{100} = \frac{\sqrt{3}}{2}a \tag{9}$$

Hence, using Bragg's law,

$$n\lambda = 2d \sin \theta \tag{10}$$

it is easy to determine *a* and *c* from the angle of the corresponding 1st order peaks,

$$c = \frac{\lambda}{\sin \theta_{002}}$$ (11)

$$a = \frac{\lambda}{\sqrt{3}\ \sin \theta_{100}}$$ (12)

where λ is the wavelength of the X-ray source. In our case, this was cobalt, with $K_\alpha = 1.7889$ Å. More details on the XRD measurement procedure will be discussed in section 2.5.2.

2.2.3 Raman-Active Modes

Wurtzite materials belong to the space group $C_{6v}^4 - P6_3mc$ and contain the following symmetry elements: [E, C$_6$, C$_3$, C$_2$, $3\sigma_v$, $3\sigma_d$]. There are 4 atoms in the primitive unit cell, leading to 12 phonon branches of which 9 are optical and 3 are acoustic, which can be described by the following irreducible relation: $\Gamma_{irred} = 2A_1 + 2B_1 + 2E_1 + 2E_2$. According to the character table for this point group, the vibrations corresponding to the Mulliken symbols A_1, E_1, E_2 are Raman active (B_1 mode is inactive), meaning that there are a total of 6 Raman modes [24]. These modes are described in Table 2.

Table 2: Summary of Raman modes of AlN

Mulliken symbol	Mode	Illustration [25]	Frequency (cm^{-1})	Ref	Allowed back-scattering geometries [24, 26]
A$_1$	LO		885 886 893	[26] [27] [28]	Z(YY)Z'; Z(XX)Z'
	TO		607 610 614	[26] [27] [28]	X(YY)X'; X(ZZ)X'
E$_1$	LO				
	TO		667 666 673	[26] [27] [28]	X(YZ)X'
E$_2$	low		249	[26]	Z(YX)Z'; Z(YY)Z'; X(YY)X'
	high		654 655 660	[26] [27] [28]	Z(YX)Z'; Z(YY)Z'; X(YY)X'

2.3 Thin Film Details

The 100 nm thick *wurtzite*-AlN thin films used in this project were grown along the *c*-axis on Si(111) by molecular beam epitaxy (MBE) using ammonia as the N precursor and a standard solid source for aluminium. The films were supplied by *EasyGan* (website: www.easy-gan.com). For more details on the growth of AlN and other group III nitrides on Si (111), please refer to [29] and [30]. The films were grown on 2" wafers which were cut into approximately 1 x 1 cm^2 shapes for the implantation.

He
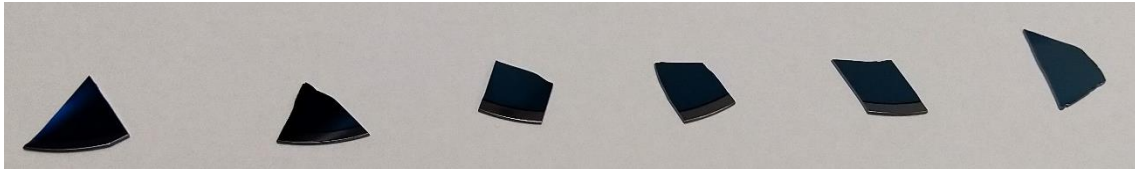
Sc
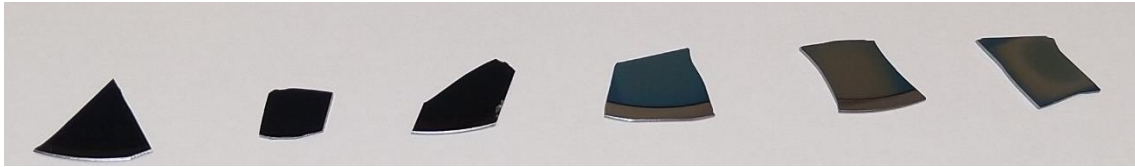
Figure 9: photos of the cut AlN samples used in the implantation. Samples are arranged from left to right in order of fluence: un-implanted, 1 x 10^{15}, 5 x 10^{15}, 1 x 10^{16}, 5 x 10^{16}, 1 x 10^{17} ions/cm^2.

In Figure 9, the photos of the cut AlN samples that were then implanted with He and Sc are presented. There is not much change in the colour of the AlN implanted with He. There is a clear transition in colour from blue to metallic grey for AlN implanted with Sc from 1 x 10^{16} to 5 x 10^{16} ions/cm^2 and above.

2.4 Implantation Procedure and Basic Physics

The samples were implanted with He$^+$ and Sc$^+$ ions at 8 keV and 30 keV, respectively. As explained in sections 3.1 (He) and 4.1 (Sc), the 8 keV energy allowed for a more uniform implantation profile for depths 50 – 100 nm, and 30 kV was the highest electric field we could generate at the time.

Released from a gas source, the ions were accelerated across an electric field and traversed through a vacuum system onto the target at normal incidence. Several focussing lenses ensured an appropriate beam width for uniform implantation across the surface. A mass analyser magnet was utilised to separate impure ions from the mixture depending on their charge and mass using the Lorentz equation. Figure 10 illustrates an implanter system similar to that used at GNS.
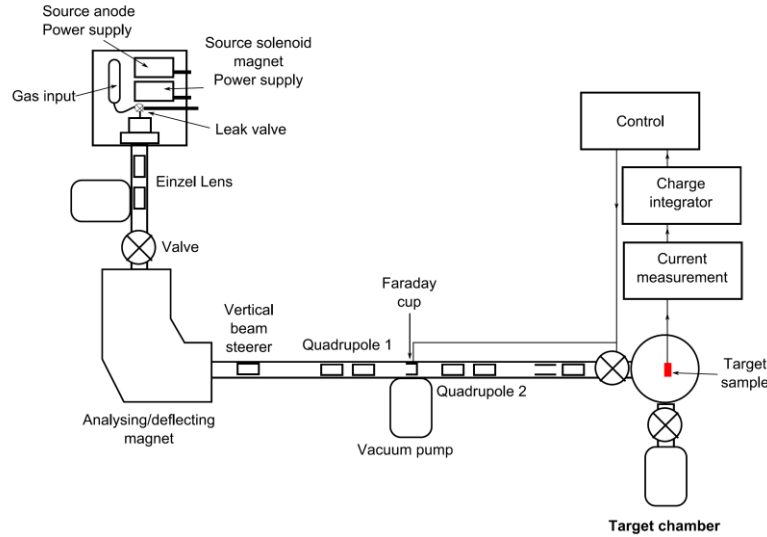
Figure 10: schematic of implanter system similar to that used at GNS [31].

The physics of ion implantation are well understood. In this thesis, we shall cover relevant aspects with information from [32]. Ion implantation is a technique whereby almost any element can be implemented into a lattice via energetic insertion. As the incident ions tunnel through the lattice they dissipate energy to their surroundings via electronic stopping and nuclear stopping,

$$S(E) = S_e(E) + S_n(E) \qquad (13)$$

where $S(E)$ is the stopping power; the rate of energy loss by the ion per unit length; and the subscripts e and n denote electronic and nuclear stopping, respectively. Electronic stopping is a continuous dissipation of energy from the ion due to Coulomb interactions with the electron clouds in the lattice. Nuclear stopping is when the ion collides with the nuclei of the atoms and is a discrete transfer of energy at each collision akin to the collision between two billiard balls. In the mass and energy regime of the ions we implanted, electronic stopping can be ignored, and the predominant energy transfer mechanism is nuclear stopping.

Nuclear collisions can be violent with large transfers of energy and angular deflections of involved nuclei. Using conservation of mass and energy principles we can calculate the energy transfer between an incident nucleus and a target nucleus,

$$T = E_0 \sin^2 \frac{\theta_c}{2} \frac{4M_1 M_2}{(M_1 + M_2)^2} \qquad (14)$$

where T is the energy transferred, E_0 is the incident ion energy, θ_c is the scattering angle in the centre of mass frame and M_1 and M_2 are the masses of the two nuclei. If the energy transferred is greater than the displacement energy ($T > E_d$), then the incident ion can displace an atom from its equilibrium lattice site, known as a primary cascade. In the simplest case, this atom will come to rest at an interstitial site elsewhere in the lattice, known as a Frenkel defect. However, at sufficient energies the displaced atom can collide with and displace other atoms, causing further cascades. Figure 11 demonstrates a typical path of an implanted ion with primary and secondary cascades as well as sputtering.
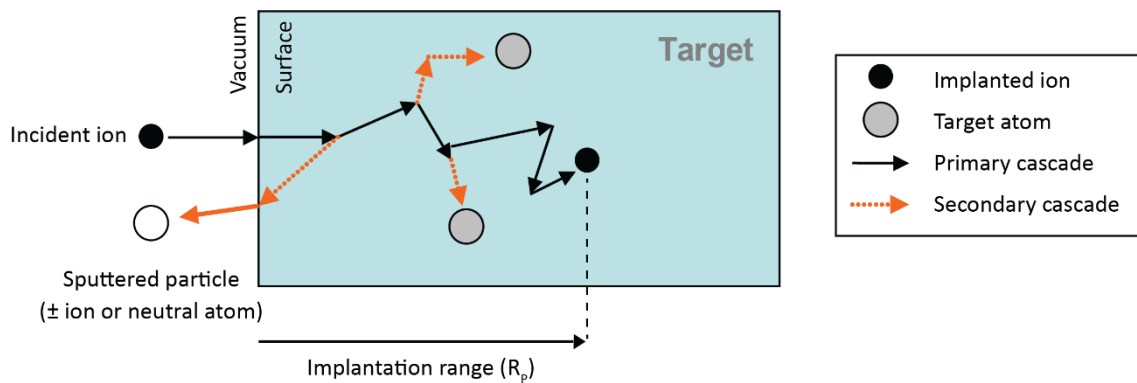
Figure 11: path of implanted ion in target with primary and secondary cascades as well as sputtering. Image adapted from [32].

In this way, the incident ion can create significant damage along the ion track in the form of vacancies and interstitial atoms. At fluences above the amorphization threshold, the damage from individual tracks can combine and form amorphous regions in the solid. Non-inert elements such as Sc can replace the Al and bond with N, forming ScN. On the other hand, inert He can cause damage, but cannot bond with the Al or N.

The stopping range is the depth at which the ion comes to rest. All ions impinging on the same material with the same energy will not follow the same path and stop at the same location because the nature of the collisions is a random process. At low fluences, the average projected range (R_P) is well described by a Gaussian distribution, but at higher doses, i.e. where the

atomic concentration is of the order of tens of atomic %, sputtering effects can significantly alter the profile.

Sputtering is the effect of atoms at the surface being ejected from collisions between the ion and near-surface atoms. The sputtering yield is defined as the number of ejected atoms per incident ion. At low doses, each ion will primarily sputter only target atoms and will itself be embedded in the lattice. At high fluences, each ion will sputter a combination of target and implanted ions. Eventually, a steady-state condition will be reached where as many implanted ions are sputtered as are replenished. This marks an upper limit of the concentration attainable for a given ion at a given energy. Figure 12 illustrates the effect of sputtering on the implantation profile as a function of fluence.

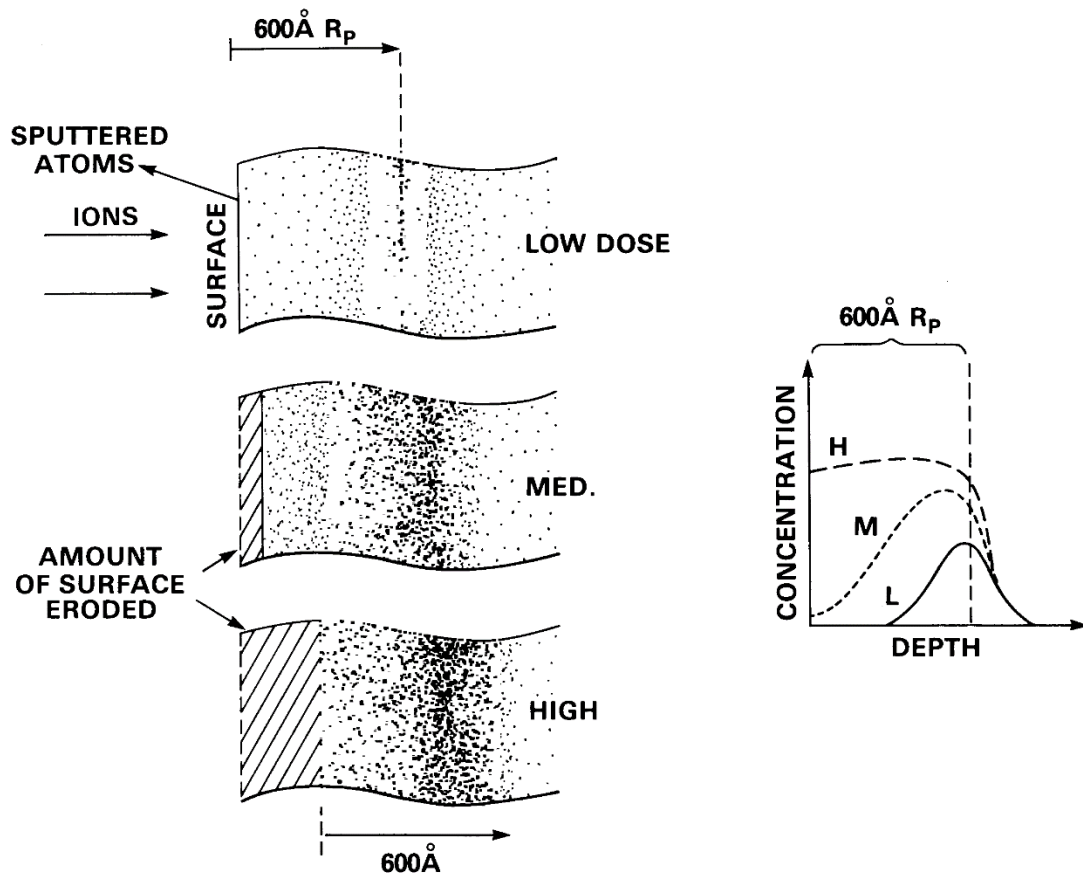Figure 12: diagram of ion concentration for low (L), medium (M) and high (H) fluences and effects of sputtering on the surface [33].

For the He and Sc implantation, DTRIM simulations were performed to obtain the implantation profile as a function of fluence. From this, we can determine the concentration in atomic % along with other useful parameters such as the sputtering yield and relative target atom ratio.

The DTRIM simulations for each ion are presented in their respective sections, 3.1 (He) and 4.1.1 (Sc).

2.4.1   Dynamic Transport and Range of Ions in Matter

The implantation of He and Sc into AlN/Si(111) system were modelled using the *Dynamic Transport and Range of Ions in Matter* (DTRIM) program [34]. DTRIM, developed by Ziegler *et al.*, is an example of a Monte Carlo (MC) program that simulates the interactions of energetic ions in matter. It provides information about ion implantation, sputtering and radiation damage among other things with good accuracy. Rather than working out the exact scattering parameters of each ion as it interacts with the target atoms, a MC approach treats the scattering as a random process with probabilistic outcomes. Accuracy is improved by taking the average value of a large number of simulated ions. For more information on MC programs, please refer to [31].

To simplify calculations, DTRIM assumes the target is amorphous, i.e. crystal orientation is neglected and the atomic arrangement is random. Additionally, each interaction between incident ion and target atom is treated as a binary collision ignoring neighbouring atoms and the ion travels in straight lines during collisions, known as the free-flight approximation [35]. The main steps in the calculation are to determine the step length between collisions, the nuclear energy loss at each collision and the new direction of motion after each collision [32]. Furthermore, DTRIM modifies the target during the calculations to account for the implanted ions and their effects on the target. This allows for an accurate calculation of various parameters such as the implantation profile, sputtering effects, damage effects and more. For a full description of DTRIM and how each parameter is determined, please refer to [36].

2.5 Experimental Techniques

2.5.1 Raman Spectroscopy

We shall now take a brief look at the technique of Raman spectroscopy and the experimental set-up used in this project in a way that is relevant for thin film analysis. The following information is sourced from [37, 38].

Raman spectroscopy is named after the Indian scientist Sir C. V. Raman who was the first person to observe inelastic scattering of light in inorganic liquids using sunlight in 1928. For his discovery, he won the Nobel Prize in Physics in 1930. Nowadays with the advancements of lasers, optics and computer technology, Raman spectroscopy is a widely used technique to characterise the composition and vibrational properties of materials. The Raman spectrum of a material is a unique signature that depends on its properties, such as its composition, structure and strain.

Raman spectroscopy is a study of the inelastic scattering of light. From a classical perspective, incident electromagnetic radiation can interact with and excite vibrational modes in molecules/atoms that re-scatter this light in all directions at a slightly different energy. The scattered light is detected by a spectrometer and the difference in energy between the incident and scattered light corresponds to the energy of the vibration. For a full treatment of the physics behind Raman scattering, please refer to the following resources [37, 38].

Experimental Set-up

Modern spectrometers use a monochromatic light source from a laser and various optical equipment to guide the beam and measure the Raman scattered light.
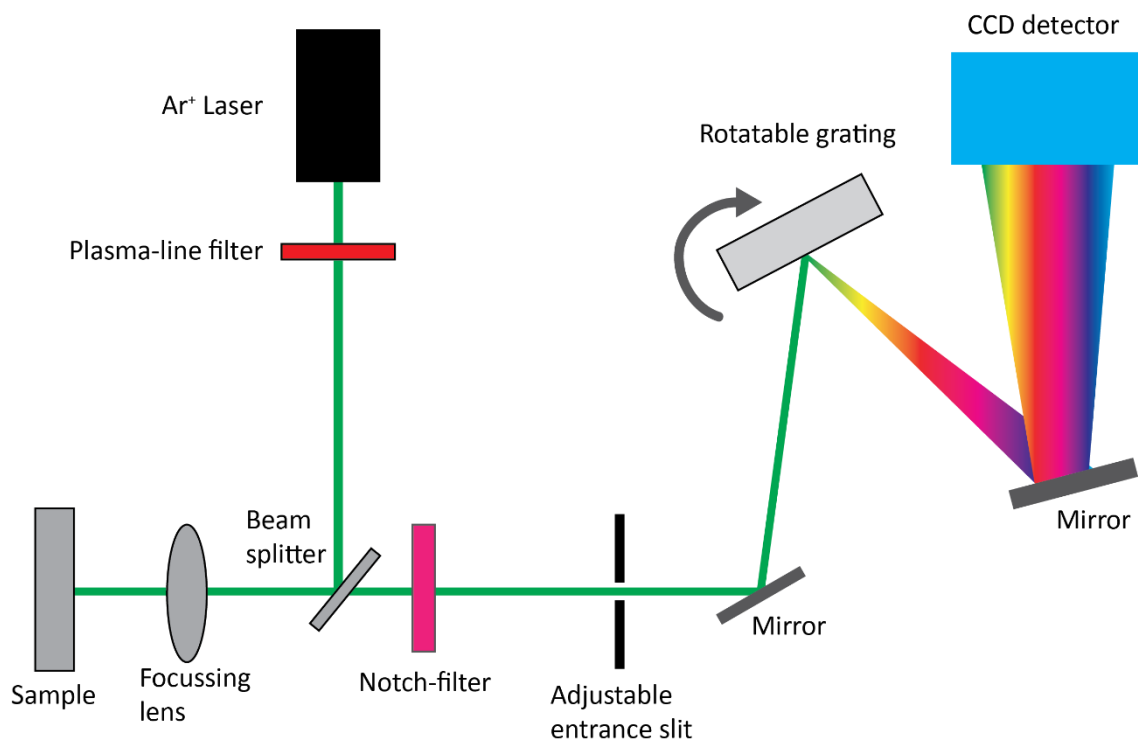

Figure 13: experimental set-up of Raman spectrometer in back-scattering geometry similar to that at VUW.

Figure 13 illustrates a typical system used in back-scattering geometry for Raman spectroscopy. A laser beam is focussed onto the surface of the sample being investigated using a microscope lens. The back-scattered light is then passed through a notch filter using a beam-splitter, where most of the high intensity Rayleigh scattered light is filtered out. The light is then shone onto a grating which disperses it based on its wavelength, determining its position when it reaches a charged couple device (CCD) detector. An adjustable entrance slit controls the amount of light reaching the grating. This is typically tuned to cut-off stray light from the environment. The choice of grating determines the range of frequencies measured by the CCD detector and the resolution. For example, in our system, we utilised an 1800 lines/mm grating which provided a 600 cm^{-1} range and a resolution of 0.5 cm^{-1}.

In our project, Raman spectroscopy was performed at Victoria University of Wellington (VUW) using the LABRAM system in back-scattering geometry parallel to the *c*-axis. There was no polarisation preference in the *xy*-plane to allow the detection of as many Raman peaks as possible in this geometry. An argon ion laser provided a reliable source of 514.5 nm (green)

light. The green laser was chosen because it was readily available and has an energy (2.4 eV) well below the band gap of AlN (6.2 eV). A laser power of 4.8 mW was high enough to improve the signal-to-noise ratio to a desired level yet low enough to not heat the sample. Furthermore, we utilised a 1800 lines/mm grating and an Olympus x100 objective, which has a numerical aperture of 0.9, for all measurements. The acquisition time was 60s, averaged 20 times to reduce noise for all measurements.

We shall now briefly go through the various ways to characterise the Raman peaks and some factors that influence them.

Intensity

The intensity of a Raman peak is influenced by many factors [37], including:

1. The number of particles scattering at that particular energy; (N is number density)
2. Intensity of incident light (I_0)
3. Raman scattering cross-section which is proportional to the 4th power of laser frequency ($\sigma \propto f^4$)
4. The scattering solid angle (Ω), related to the lens optics
5. Temperature dependent factors relating to the spectral width, resolution of the detection system and the investigated molecule ($F(T)$)

$$I \propto NI_0\sigma\Omega F(T) \tag{15}$$

In our measurements, all experimental parameters were kept the same, so the changes in Raman intensities are related to the number of particles coherently contributing to the Raman mode.

Shifts in Peak Position

The frequency of a Raman peak can change due to stress/strain. For Raman scattering in a crystal structure, biaxial stress can shift the frequency of the peak,

$$\Delta\omega = k\sigma_\perp \tag{16}$$

where $\Delta\omega$ is the change in phonon frequency, k is the Raman stress factor (constant for a given mode and material) and $\sigma_\perp$ is the stress perpendicular to the growth axis [26]. Changes in the frequency of the Raman peak can help identify stress/strain states in the material.

Linewidth

Broadening of Raman peaks is the result of a reduction in the phonon mean free path or phonon lifetime [39]. As a phonon propagates through the lattice, it naturally disperses, resulting in a spread in frequency or energy space. The width of a Raman peak essentially characterises the amount of time before a phonon decays; the linewidth is inversely proportional to the phonon lifetime [39]. A phonon terminates when it encounters a change in the structural properties such as that from lattice defects, foreign elements or a grain boundary [40]. Therefore, sharp Raman peaks suggest good crystalline order or large crystal sizes, whereas broad peaks could be an indication of a large concentration of defects or small grain sizes. It has been reported in literature that increasing lattice disorder or reducing grain size increases the linewidth [40-43].

2.5.2 X-Ray Diffraction

The background information on X-ray diffraction (XRD) is sourced from [44]. XRD is a non-destructive technique used to measure the internal structure of materials, such as crystal structure and orientation, composition and texture. Applied to thin films, we can use XRD to confirm the preferred growth orientation, crystal symmetry and the *a* and *c* lattice parameters.

Electromagnetic radiation in the X-Ray range will be diffracted by atoms in a lattice in all directions because the wavelength is of a similar size to the atomic spacings. Most of the diffracted rays will destructively interfere, however constructive interference will occur for X-Rays reflecting off crystallographic planes that obey Bragg's law. Figure 14 illustrates this principle.
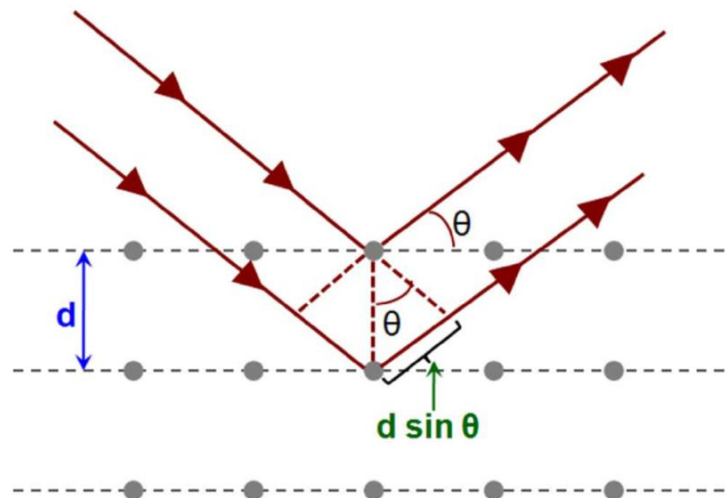

Figure 14: X-ray reflection off two adjacent lattice planes. Image taken from [45].

The path difference between two X-Rays reflected off adjacent planes with the same incident and out-going vectors is $2d \sin \theta$, where d is the distance between the planes and θ, the angle between the X-ray and the planes. Constructive interference will occur when the path difference is an integer number of wavelengths,

$$n\lambda = 2d \sin \theta \qquad (17)$$

where n is an integer and λ is the wavelength. Equation (17) is known as Bragg's law, after Sir William Bragg derived this condition in 1913.

Measurement Scans
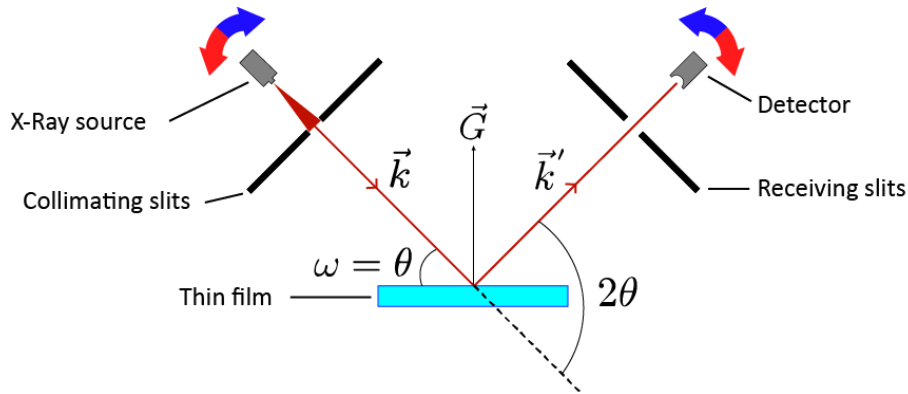
$2\theta - \omega$ scan

Figure 15: $2\theta - \omega$ scan geometry. $\vec{k}$ and $\vec{k}'$ are the incident and out-going wavevectors, respectively. $\vec{G} = \vec{k}' - \vec{k}$ is the reciprocal lattice vector for the d_{hkl} planes.

$2\theta - \omega$ scans are one of the main techniques used in XRD. The source and detector are set up such that 2θ is twice ω. The source and detector are then rotated around the sample to conserve this condition. When $\omega = \theta$, the Bragg condition is satisfied, and a diffraction peak will occur. Therefore, for non-oriented samples, such as powdered samples, or polycrystalline films with randomly oriented grains, many peaks will be observed. However, for films grown along a preferential axis, a large peak is expected, and this can be used to verify the growth direction. Additionally, higher order peaks corresponding to $n = 2, 3$ etc. may be observed and will be of lower intensity.

This geometry allows for the determination of d_{hkl} lattice spacings via Bragg's law and can be used to determine the lattice parameters of the crystal. Variations in the spacings due to inhomogeneous strain will cause broadening of the peak, whereas homogeneous strain will move the entire peak.
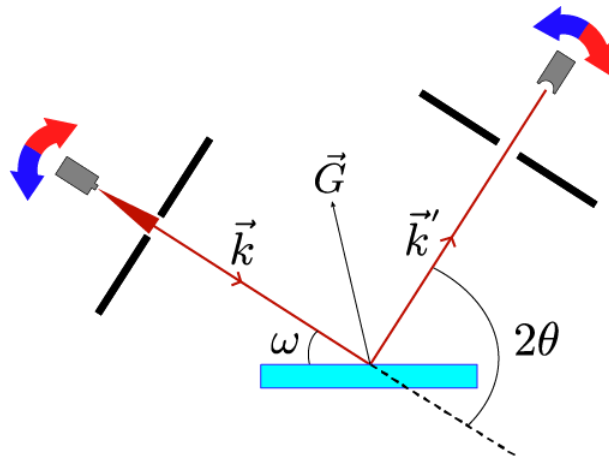
Rocking curve

Figure 16: General rocking curve or ω scan. The diagram is exaggerated for illustrative purposes.

The rocking curve, also known as ω scan, is another main XRD technique and often goes complimentary to the $2\theta - \omega$ scan. This scan is useful when the preferred crystal orientation is known. The source and detector are initially set-up for a known diffraction peak and 2θ is twice ω. The source and detector are then moved in unison to fix the angle between them. The effect is to "rock" the sample back and forth, hence the name. d_{hkl} lattice planes oriented slightly off-axis will be brought into alignment by the rotation of the sample and contribute to the peak.

A powdered sample has no preferred orientation and will therefore have no change in intensity in the rocking curve. In the case of films, the presence of a peak confirms a preferred orientation of lattice planes. The width of the peak determines the variation in grain orientation around the measurement axis. Therefore, this technique is ideal for determining the texture of a film.

Experimental Procedure

XRD was performed at Callaghan Innovation under the supervision of Bridget Ingham. We utilised a Rigaku SmartLab instrument in parallel beam geometry for in-plane and out-of-plane measurements with a HyPix 3000 detector. In the out-of-plane geometry, the detector was used in 1D collection mode with an incident slit height of 1 mm. In the in-plane geometry, the detector was used in 0D collection mode with 0.5° Soller slits and 1 mm incident and receiving slits. The X-ray source was cobalt, with $K_\alpha = 1.7889$ Å. There is also a small amount of K_β present (1.6208 Å), leading to several peaks marked in Figure 17.

For out-of-plane measurements the instrument is set up in the usual way; the sample is placed on a horizontal stage with the *c*-axis vertical and the source/detectors are elevated above the surface. Since the *c*-axis orientation is known, it is easy to align the instrument.

Initially, a broad scan is taken to obtain an overview of the diffractogram of AlN, the substrate and any other instrumental peaks.
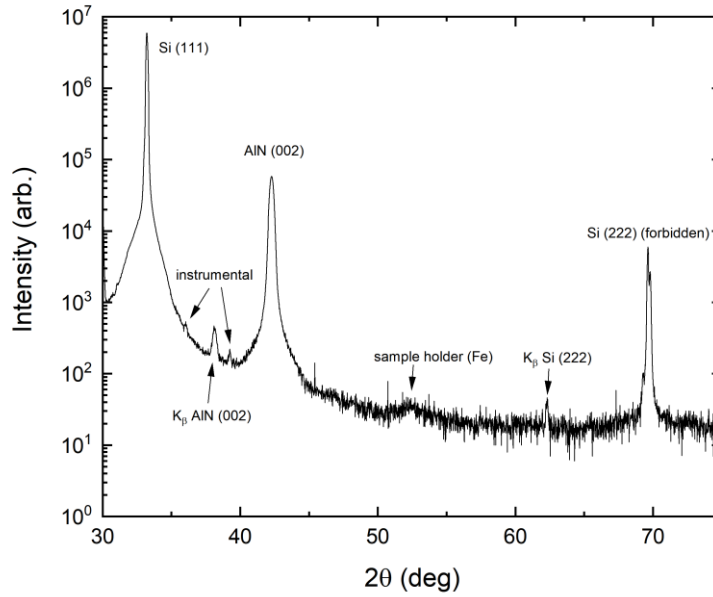

Figure 17: full $2\theta - \omega$ scan out-of-plane of AlN with cobalt source.

The Si (111) peak at 33.19 º has an intensity many orders of magnitude higher than any other peak in the spectrum. On a logarithmic scale we can clearly see the AlN (002) peak at 42.28 º and its K_β at 38.13 º along with the forbidden Si (222) peak at 69.78 º and its K_β at 62.30 º. Additionally, there are other minor instrumental peaks and a small peak at 52.40 º corresponding to iron in the sample holder. The fact that we can only see the (002) corresponding to AlN shows the high *c*-axis orientation of the film.

Regarding the in-plane procedure, although the *c*-axis direction is known, the sample has an arbitrary rotation in the basal plane. Thus, more steps are required to align the instrument for this procedure.
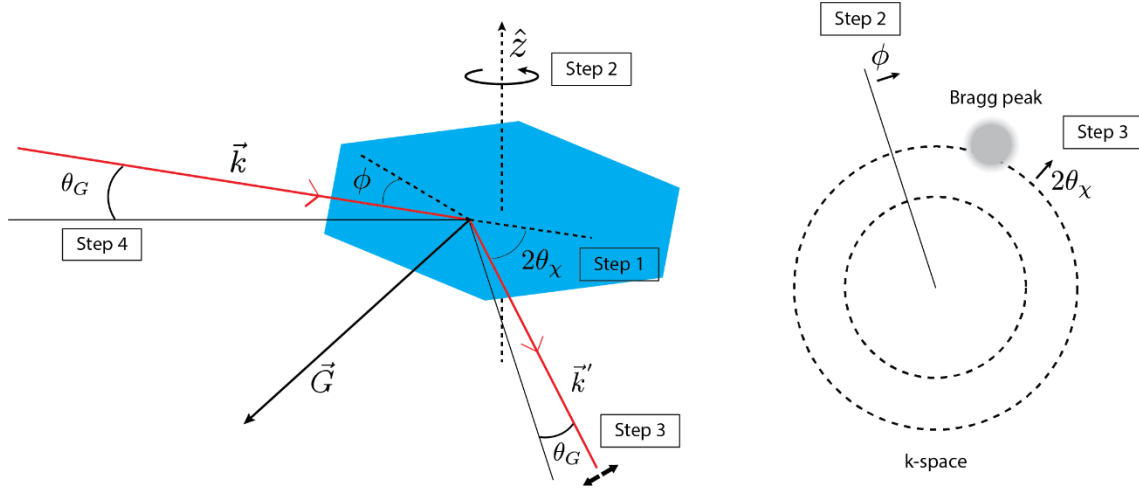
Figure 18: diagram of in-plane XRD alignment procedure (left) with effect of alignment on k-space (right); blue hexagon represents the AlN film and its hexagonal-like structure.

Step 1: Set $2\theta_\chi$ to that of the desired peak. Also, set a reasonable value for grazing incidence $\approx 1^o$.

Step 2: Rotate the sample about the z-axis. This varies ϕ and a Bragg peak will occur when $\phi = \frac{1}{2}2\theta_\chi$.

Step 3: Fix the source and move the detector to refine the intensity of the Bragg peak for optimal signal.

Step 4: Adjust the grazing incidence (θ_G) until maximum intensity is obtained.

Step 5: Repeat $2\theta_\chi - \phi$ and ϕ scans as $2\theta - \omega$ and ω scans as for the out-of-plane measurements.

To observe the AlN (100) peak, the initial $2\theta_\chi$ value chosen was 38.6°. Due to the hexagonal symmetry of the wurtzite structure, we would expect Bragg peaks of approximately the same intensity every 60°, which is exactly what we observed (see Figure 19). The effect of varying ϕ and $2\theta_\chi$ in k-space is shown in Figure 18 (right). Changing ϕ follows a circular path that keeps the value of k constant, effectively rotating it about the origin. Changing $2\theta_\chi$ on the other hand varies the radius of these circles, changing the magnitude of k. To get the best alignment, we wish to be at the centre of the Bragg peak for maximum intensity.
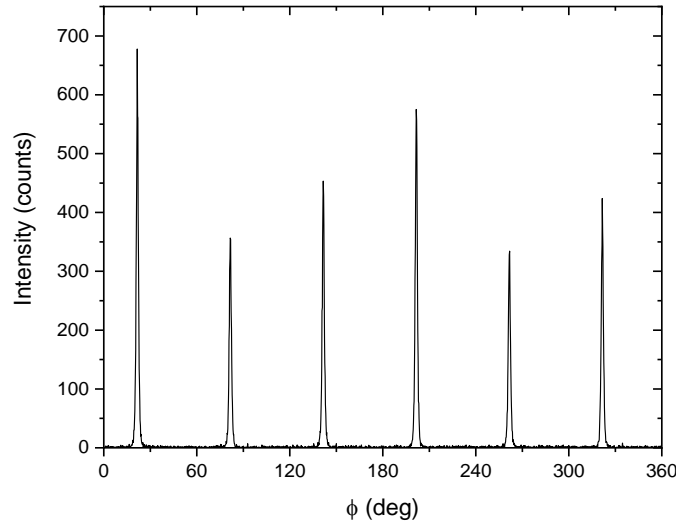
Figure 19: {100} planes, ϕ scan of AlN over 360° range, revealing 6 peaks that are 60° apart.

2.5.3 Atomic Force Microscopy

Atomic force microscopy was performed on the AlN films to determine the surface topography. This involves using a tip attached to the end of a cantilever that is scanned across the material's surface. The cantilever will be deflected up and down as moves, depending on the topography it is measuring. A focussed laser is reflected off the top of the cantilever and onto a photodiode detector, which tracks its movement. The instrument detects changes in the laser's position on the photodiode to determine the topography. This allows for extremely sensitive measurement of surface properties [46]. Figure 20 shows a simple schematic for an AFM system.
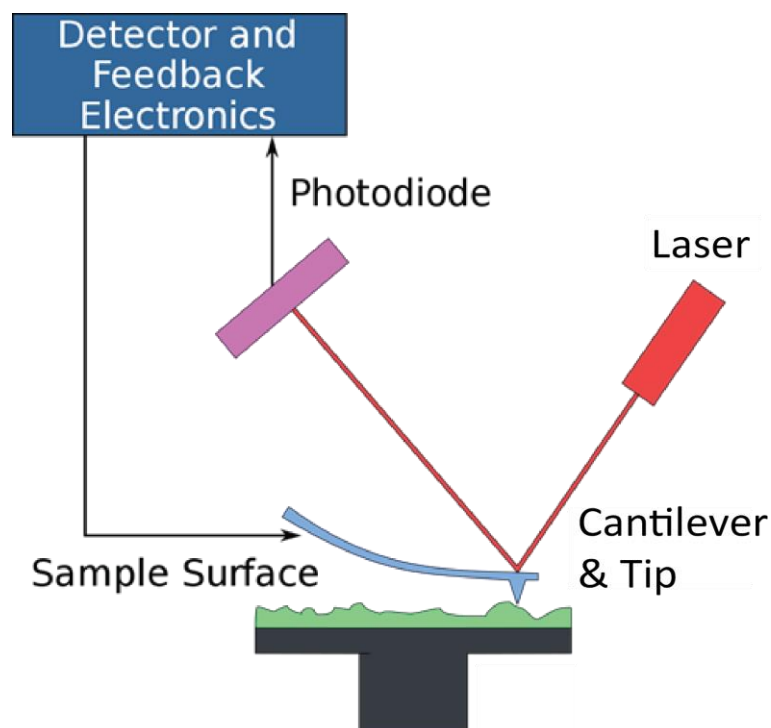
Figure 20: simple diagram showing arrangement of the laser, cantilever and tip, photodiode and sample for AFM measurement.

We conducted various 2 x 2 and 5 x 5 μm^2 scans at 256 x 256 resolution with the nanosurf "PPP_NCHR" tip - a silicon coated tip designed for tapping mode AFM. This tip has a radius < 10 nm, allowing a resolution of 20 nm, with a height of 10 – 15 μm. The mechanical Q factor for the tip employed was 375 and a spring constant of 17 N/m, in the medium range for stiffness.

The topography was analysed using Gwyddion software version 2.53. The images were treated to reduce line mismatching and an artificial background from the instrument. There is minor surface contamination/streaking in some of the samples. These regions are ignored in all roughness calculations.
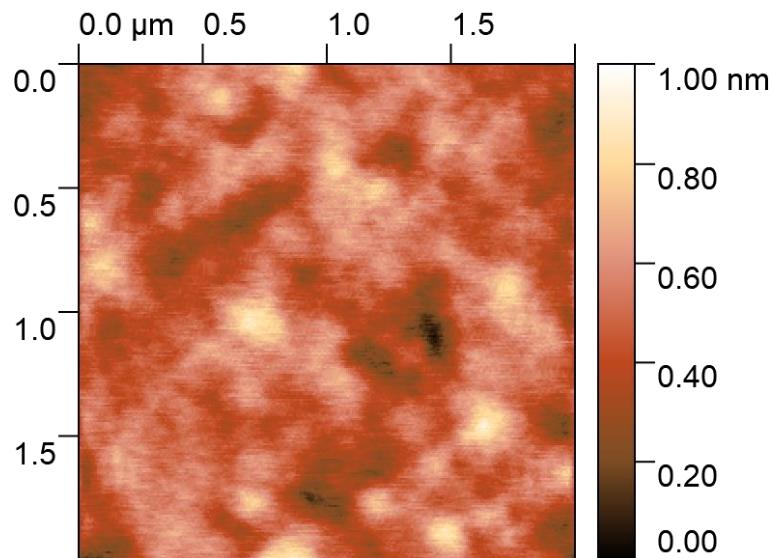
Figure 21: 2 x 2 μm^2 AFM image of AlN (un-implanted).

The 2 x 2 μm^2 scan (Figure 21) has an RMS surface roughness of 0.13 nm, indicating a very smooth surface in this region. The contrasting dark and light regions illustrate the topography of the film. The supplier has conducted AFM on similar films, illustrating steps and terraces as well as threading dislocations through the surface [47, 48]. Unfortunately, with the tip we employed and due to noise we were unable to get as high a resolution to observe these.

Undoped, $S_q = 0.19$ nm

He_AlN_1E15, $S_q = 0.22$ nm

He_AlN 1E16, $S_q = 0.24$ nm

He_AlN_1E17, $S_q = 0.21$ nm

Sc_AlN 5E16, $S_q = 0.32$ nm

Sc_AlN 1E17, $S_q = 0.78$ nm

Figure 22: AFM images of AlN implanted with He and Sc for various fluences (ions/cm^2). Each image is 5 x 5 μm^2 in size. Please note for the contaminant on top-right corner of Sc 1 x 10^{17} ions/cm^2 has been ignored.
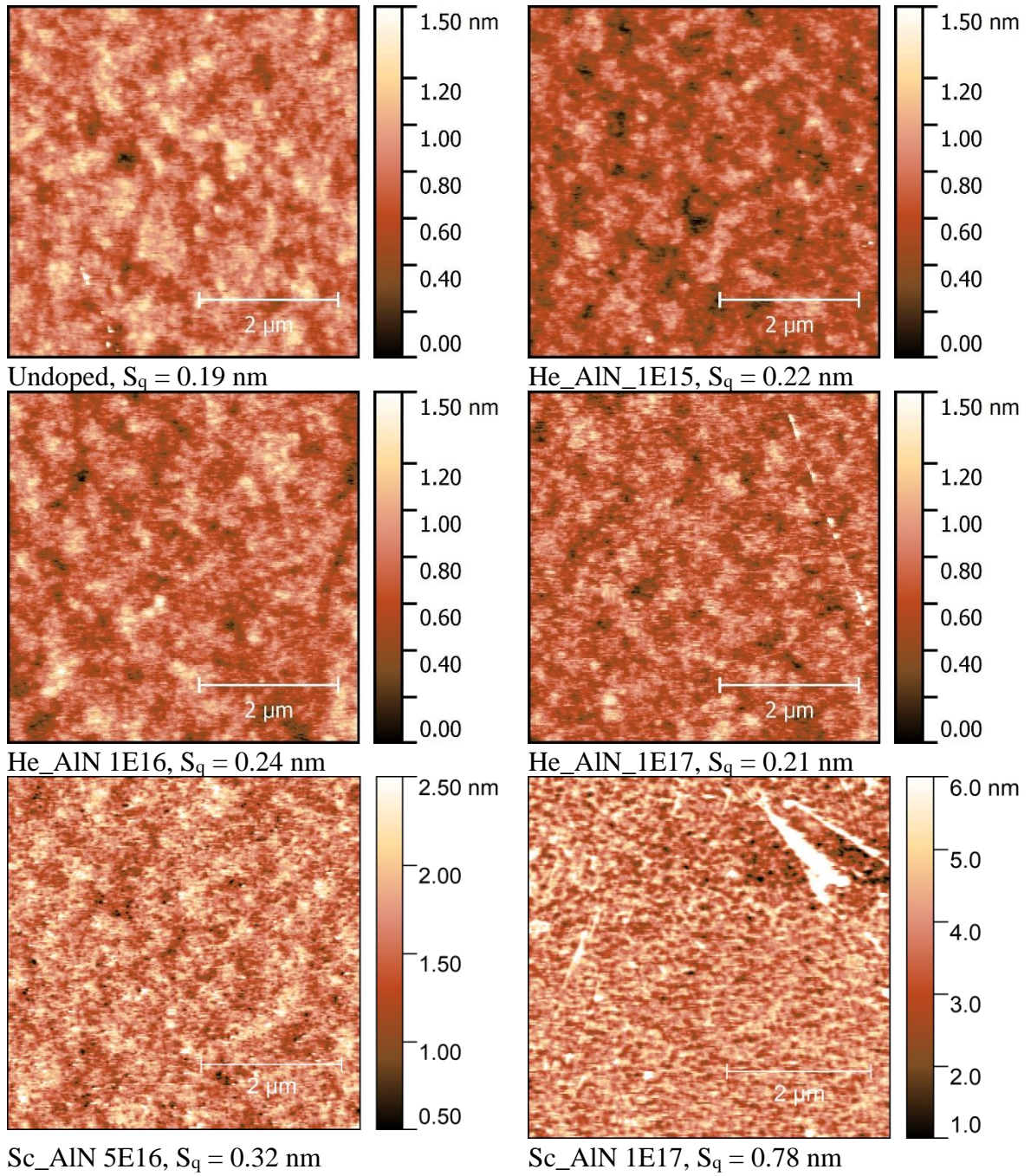
The RMS surface roughness are listed in Figure 22. At 5 x 5 μm^2 the films are very smooth with an RMS surface roughness of 0.19 nm. We do not observe any major changes in the surface topography from the He implantation.

For the Sc implanted samples, we see that the surface topography looks different to un-implanted. The implanted samples look more granular-like, likely due to accumulation of Sc on the surface. Overall, the films are still smooth with an RMS surface roughness of 0.78 nm for AlN implanted with Sc at a fluence of 1 x 10^{17} ions/cm^2.

2.5.4   Piezoelectric Force Microscopy

PFM is a relatively new technique that applies AFM in a specialised way. The process of PFM is very similar to AFM. In addition, an alternating voltage is applied to a conductive tip/cantilever when in contact with the sample surface. The sample is grounded at the base, creating an electric field across it. This allows the cantilever to be deflected by the material's piezoelectric response and thus allows for analysis of its electromechanical properties. The change in the c-lattice parameter (Δc) is linear with applied voltage (V), with the proportionality constant being d_{33} [11],

$$\Delta c = d_{33} V \tag{18}$$

In our system an electric field is applied in the c-axis and deflections are most sensitive in this axis, measuring the d_{33}. In addition to the piezoelectric response, there will be electrostatic attractions between the tip and surface, so the overall deflection is a combination of the two.

Experimental Details

We utilised a Nanosurf FlexAFM system for our measurements. The conductive tips were made of Si with a platinum silicide (PtSi) coating (radius < 20 nm). These had spring constants in the range 33 – 40 N/m, resonant frequencies of 270 – 300 kHz and Q factors of 500 – 600. The tip was held stationary in contact during measurements, known as static mode. The applied frequency was 1 kHz, which is well below the resonant frequency of the tip and above that of background vibrations. It also offers the least instrumental noise.

The samples were attached on a grounded metallic stage using carbon tape. Multiple locations on the surface were probed. At each location, the AC voltage was manually ramped up from 0 to 10 V in 2 V increments. The machine recorded 1024 data points in the span of 5s for a

particular voltage. This provides a large sample size suitable for data analysis. Each data point consists of an amplitude and a phase reading.

Measurements were only taken near the centre of each sample to reduce edge effects which have shown to reduce the measured d_{33} [49]. Furthermore, as a reference, strontium titanate (STO) was measured before AlN and we report deflections in the range $50 - 60$ pm/V, an order of magnitude larger than any obtained by AlN, which indicates we are indeed observing a piezoelectric response. STO is known to have a high piezoelectricity and has been reported to have a d_{33} of the order of tens of pm/V [50].

The PFM results and analysis are presented in sections 3.2.3 (He) and 4.2.5 (Sc).

Chapter 3 AlN Implanted with He

The AlN thin films implanted with He were characterised using Raman spectroscopy, XRD and PFM. In this chapter we will examine the experimental results and analyse them to see the impact of the implantation on the structural, vibrational and piezoelectric properties, namely the strain, damage and effect on d_{33}. The methodology and important parameters used in each technique are discussed, followed by an analysis and conclusion. Firstly, we shall discuss the DTRIM simulations.
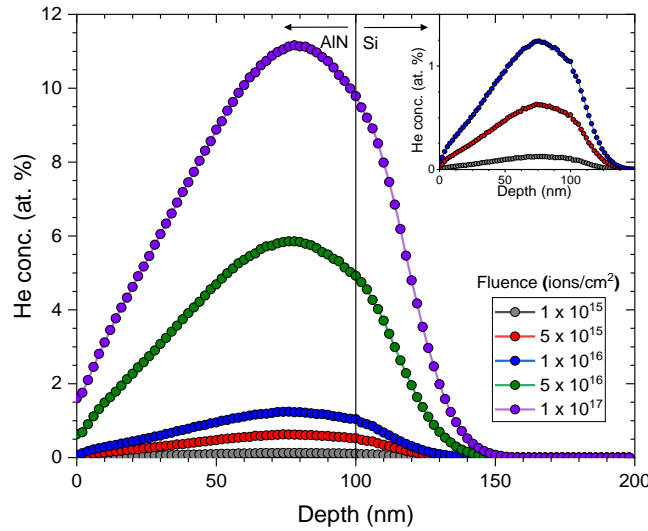
3.1 Dynamic Transport and Range of Ions in Matter

Figure 23: Implantation profile of He in AlN/Si(111) each 100 nm thick for 8 keV at various fluences (ions/cm^2). The inset is a magnification of the fluences up to 1 x 10^{16} ions/cm^2.

He$^+$ ions were implanted into AlN at 8 keV at normal incidence using the GNS implanter. The target is modelled as a dual-layer system. The first 100 nm depth is AlN ($\rho = 3.26$ g/cm^3), then from 100 nm – 200 nm it is Si ($\rho = 2.33$ g/cm^3), to match the actual sample implanted as closely as possible. Approximately 25% of the deepest He stops inside the substrate. This allows for a more uniform profile in the range 50 nm – 100 nm inside AlN as it covers the broad peak. The implantation profile looks like an asymmetric Gaussian due to a surface build-up of He. From DTRIM, the implantation range is 69 nm for all fluences and the FWHM is 80 nm.

3.2 Experimental Results and Analysis
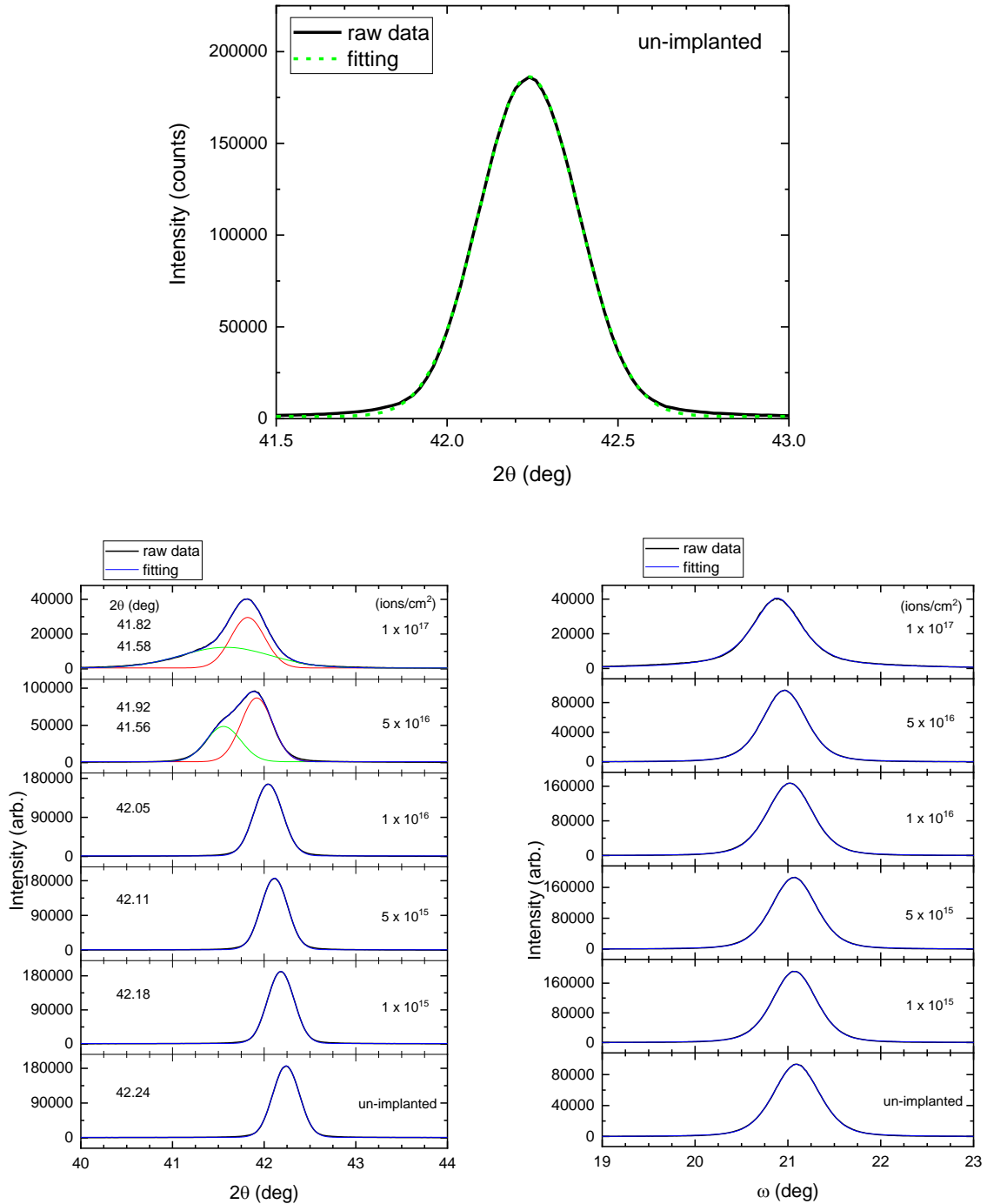
3.2.1 X-Ray Diffraction

Figure 24: out-of-plane XRD scans around (002) peak of AlN (He implanted); (top) $2\theta - \omega$ scan of un-implanted; (left) $2\theta - \omega$ scan for each fluence with peak position noted; (right) rocking curve for each fluence with FWHM noted. For the top graph, the black line is the raw data and the green dashed

line is the fitting. For the left and right graphs, the black line is the raw data and the blue line is the fitting; additionally the red and green curves for the fluences of 5 x 10^{16} and 1 x 10^{17} ions/cm^2 are the individual Gaussian fits for the double peak.

The $2\theta - \omega$ scans and rocking curves of the (002) and (100) peaks for the implanted AlN thin films are presented in Figure 24 and Figure 25, respectively. We were able to obtain good Gaussian fits for the $2\theta_{002}$ peak, suggesting strain broadening in the [002] direction. For un-implanted to a fluence of 1 x 10^{16} ions/cm^2 a single Gaussian fit was required, however, for high fluences of 5 x 10^{16} and 1 x 10^{17} ions/cm^2 a double Gaussian fit was required.

For un-implanted, the $2\theta_{002}$ peak is at 42.24^o with a FWHM of 0.34^o, corresponding to $c = 4.96 \pm 0.01$ Å. This is close to 4.98 Å reported in [51, 52], calculated using equation (11). The small FWHM of 0.34^o indicates a low-level of inhomogeneous strain in the c-axis. The $2\theta_{002}$ peak shifts to lower values with increasing fluence, indicating the implantation causes tensile strain (expansion) along the c-axis.

At higher fluences of 5 x 10^{16} and 1 x 10^{17} ions/cm^2 the bimodal distribution indicates two regions of different strain. The main peak at the higher value follows the same trend as the lower fluences and there is a smaller peak at a lower 2θ. Bimodal distributions are observed in the XRD peaks for $Al_xGa_{1-x}N$ alloy thin films and GaN implanted with inert Ar at similar fluences [14, 53]. They attribute broadening of the main peak to be caused by point defects and stacking faults and the occurrence of the lower peak to be from bubbles/voids of Ar or N, as verified by transmission electron microscopy (TEM). We were unable to perform TEM on the samples within the timeframe as it is a destructive technique. Although TEM is necessary to verify the structure, we can still have ideas of the origin of these changes. The lower peak we observe could be from an accumulation of He inside the lattice creating a highly strained region, which we observe for fluences larger than 1 x 10^{16} ions/cm^2. This fluence can therefore be a threshold beyond which a dual-phase system forms.

Regarding the (002) rocking curve in Figure 24, a pseudo-Voigt with constant FWHM was employed and provided a very good fit to the data. The pseudo-Voigt fit better than a Gaussian curve and provided more accurate values for the FWHM. The small FWHM indicates only ~0.7^o angular spread in grains about c-axis for all fluences. There is no measurable change in the FWHM with fluence.
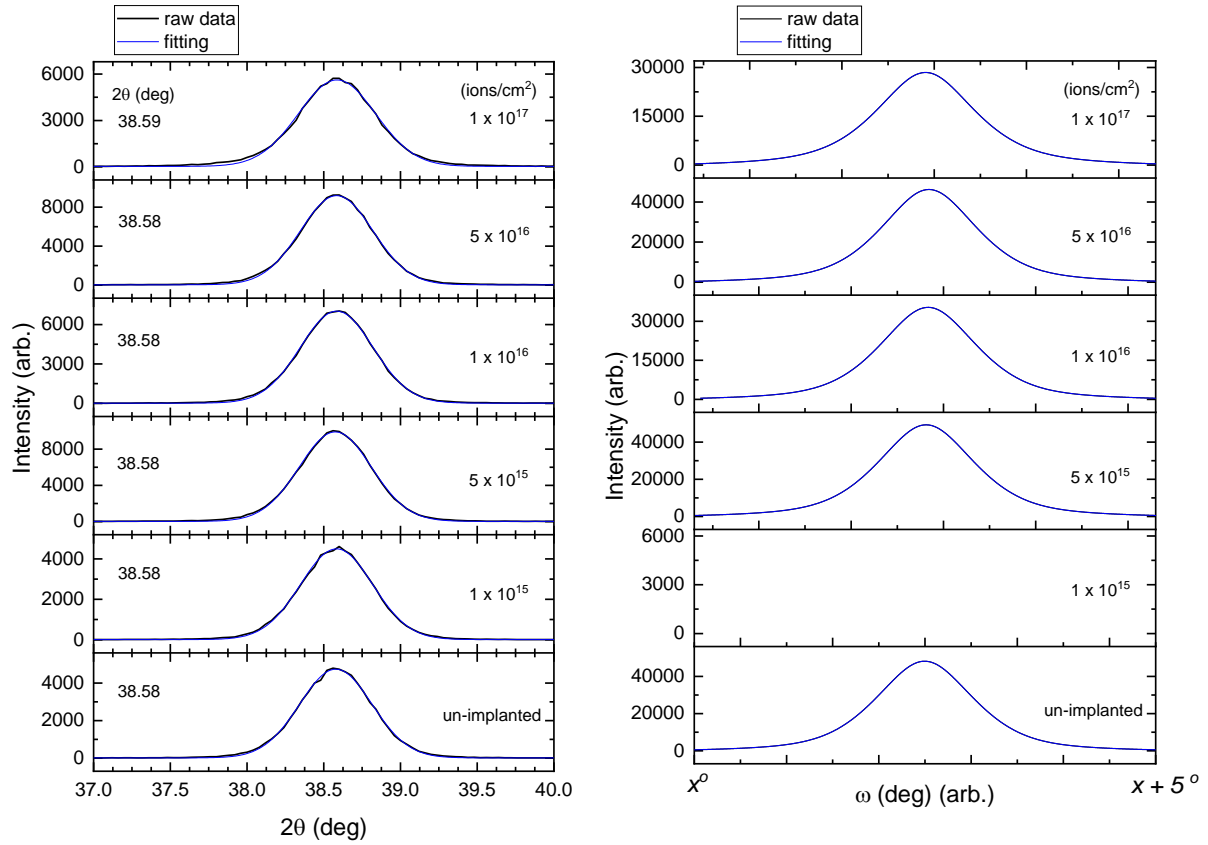
Figure 25: in-plane XRD scans around (100) peak of AlN (He implanted); (left) $2\theta - \omega$ scan with peak position noted; (right) rocking curve. *Note: the x-axis of the rocking curve is arbitrary for this peak because the sample is randomly rotated in the basal plane, i.e. there is no reference for this crystallographic direction, as opposed to the (002) peak where the c-axis is vertical.*

In-plane measurements reveal information on the crystal structure in the basal plane. Due to experimental difficulties, we were unable to obtain rocking curve data for a fluence of 1×10^{15} ions/cm^2. Using a Gaussian fitting function, we find the $2\theta_{100}$ occurs at 38.58° with a FWHM of 0.56°, corresponding to $a = 3.13 \pm 0.03$ Å, agreeing with 3.11 Å reported in [51, 52]. There is no change in the position of this peak with fluence, indicating no strain imposed on the lattice by the implantation in the basal plane. Additionally, the FWHM is 0.56° for the un-implanted sample which does not change appreciably with fluence.

An interesting observation is that the mean a lattice parameter is (slightly) 0.02 Å larger than that reported in literature and the mean c lattice parameter is (slightly) 0.02 Å smaller. This suggests there may be some biaxial strain in our 100 nm thin films from the substrate, due to the lattice mismatch between AlN and Si (111) and the thermal expansion coefficient difference.

The (100) rocking curve is fitted using a pseudo-Voigt in the same way as that for (002). The FWHM for un-implanted is 1.48°, approximately 3x larger than for (002), indicating slightly more variation in grain orientation in the basal plane. There is no broadening of this peak with fluence.
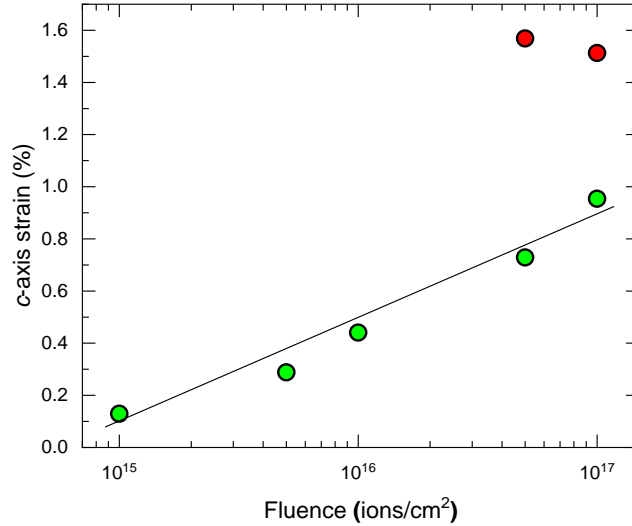

Figure 26: *c*-axis strain as a function of fluence for AlN implanted with He.

The *c*-axis strain was determined as a function of fluence using the fitting of the $2\theta - \omega$ scans in Figure 24. For the two highest fluences of 5 x 10^{16} and 1 x 10^{17} ions/cm², the strain is determined individually for the two deconvoluted fits. We observe a continuous increase in *c* lattice parameter with fluence from 4.96 Å (un-implanted) to 4.99 Å (1 x 10^{16} ions/cm²) to 5.01 Å (1 x 10^{17} ions/cm²). There is no change in *a* lattice parameter. Thus, the strain is uniaxial and the *c/a* ratio increases. This suggests that the *c*-axis is more susceptible to changes than the *a*-axis in accordance with the observations in [14] and could be because the *a*-axis is 'locked' to the substrate whereas the growth direction is in the *c*-axis; also the implantation direction is in the *c*-axis.

The strain in the *c*-axis is calculated as follows,

$$\varepsilon = \frac{c_{calc} - c_0}{c_0} \tag{19}$$

where c_0 is the lattice parameter for un-implanted AlN and c_{calc} is the lattice parameter determined by the position of the $2\theta_{002}$ peaks.

Furthermore, the uniaxial strain is plotted on the right-hand-side of Figure 26. The strain increases linearly with the log of fluence. There is minimum strain of 0.13% for 1 x 10^{15} ions/cm^2; moderate strain of 0.44% for 1 x 10^{16} ions/cm^2; maximum strain of 0.95% for 1 x 10^{17} ions/cm^2.

3.2.2   Raman Spectroscopy
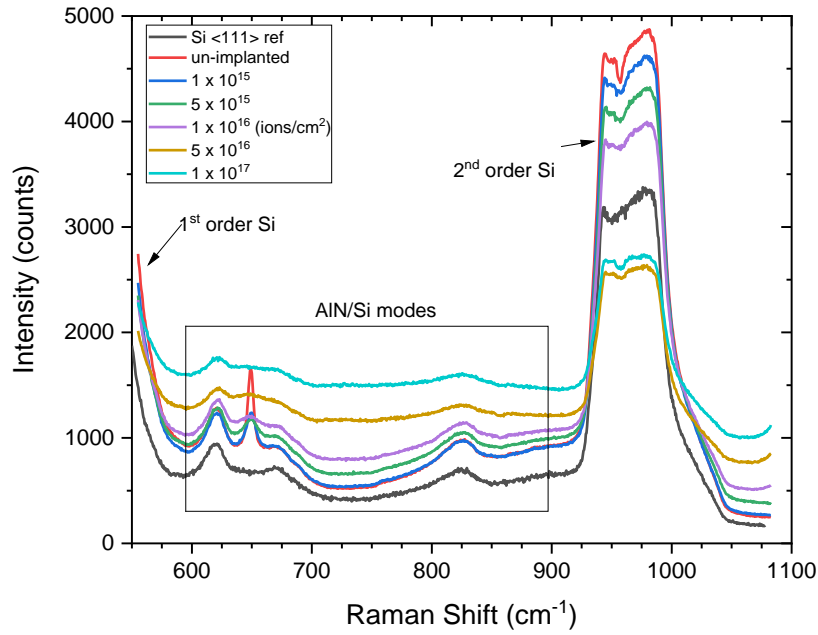
Figure 27: raw data from Raman spectroscopy of Si (111) reference and implanted AlN (He) at various fluences.

The Raman spectroscopy performed on the AlN/Si system reveals modes corresponding to the AlN film and the Si substrate. Initially, the 1st order Si peak corresponding to $O(\Gamma)$ at 520 cm^{-1} was probed for all fluences to provide a reference and ensure the instrument was calibrated correctly. In Figure 27, we can see the Raman spectra for the AlN thin film and Si (111) substrate in the range 540 – 1075 cm^{-1}. Peaks corresponding to AlN and low-intensity Si modes between 600 – 900 cm^{-1} are plotted in closer detail in Figure 28. There is a non-linear background which curves downwards then upwards smoothly that is from the Si (111) substrate.

Figure 28: Raman spectra of Si (111) and AlN implanted with He at various fluences.
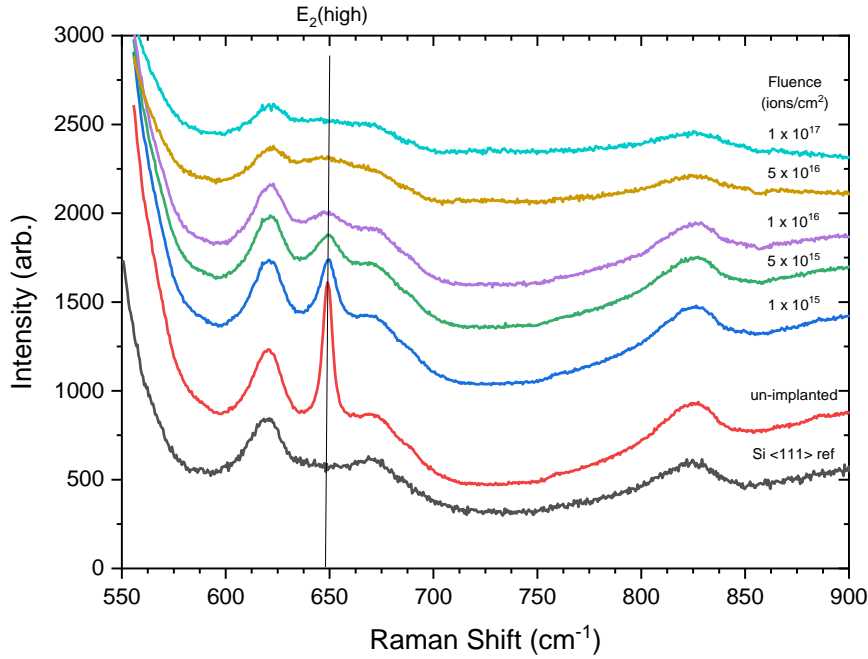
We can clearly see 4 Raman peaks. We assign the peaks at 621, 672 and 824 cm^{-1} to low intensity Si modes reported in [54]. To support this, Prokofyeva *et al.* performed Raman spectroscopy on *c*-axis oriented AlN on Si(111) and obtained a very similar background with features at 620 and 830 cm^{-1} being assigned to the Si substrate [26]. In back-scattering geometry parallel to the *c*-axis, only the E$_2$(high) and A$_1$(LO) from *c*-axis oriented AlN should be observed [26, 55]. The E$_2$(high) is expected around 655 – 660 cm^{-1} and the (lower-intensity) A$_1$(LO) around 885 – 895 cm^{-1} [26-28]. The sharp peak at 649 cm^{-1} is assigned to E$_2$(high). This value is approximately 5 – 10 cm^{-1} lower than literature which is likely due to biaxial stress from the Si substrate, which has shown to red-shift the E$_2$(high) mode in 800 nm thick AlN films on Si (111) [26]. We do not see the A$_1$(LO) peak, possibly due to a low intensity.

Table *3* summarises the E$_2$(high) peak position for AlN in our work and in literature of thin film AlN on Si.

Table 3: measured E$_2$(high) peak position. * refers to our data (un-implanted).

Raman mode	Central frequency (cm^{-1})	Reference
E$_2$(high)	649.1 ± 1.2*	
	654	[26]
	655	[27]
	660	[28]

It was difficult to fit the E_2(high) peak with a function such as Lorentzian likely due to the overlapping Si modes. The error was estimated by the width at the top of the peak plus the instrumental resolution of 0.5 cm^{-1}.

We can see a dramatic decrease in the E_2(high) peak intensity and, simultaneously, an increase in its FWHM with fluence. There is no change in the position of the peak as a result of the implantation.

The reduction in peak intensity can be attributed to a decrease in the number of atoms contributing to Raman scattering, likely due to distortion of the Al-N bonds from the implantation. The broadening of the peak suggests a decrease in the phonon mean free path, another indication of damage. It is not possible to resolve the E_2(high) mode after a fluence of 1×10^{16} ions/cm^2, which could serve as a threshold before implantation causes too much damage. Table 4 documents the E_2(high) peak intensity as a function of fluence. A spline was modelled to fit the background spectrum for each sample and subtracted off. The height of the E_2(high) peak after the subtraction was taken as its intensity.

Table 4: peak intensity of E_2(high) for AlN implanted with He at various fluences

Fluence (ions/cm^2)	E_2 (high) peak intensity (counts)
Un-implanted	1030
1×10^{15}	590
5×10^{15}	440
1×10^{16}	340
5×10^{16}	N/A
1×10^{17}	N/A

Furthermore, stress in the basal plane is expected to shift the position of the E_2(high) peak using the following relation [26],

$$\Delta\omega = k\sigma_\perp \tag{20}$$

where $\Delta\omega$ is the change in phonon frequency, k is the Raman stress factor (-6.3 ± 1.4 cm^{-1}/GPa for E_2(high) of AlN) and $\sigma_\perp$ is the stress perpendicular to the growth axis. In our case the growth axis is the c-axis and the a-axis is perpendicular to it. Therefore, the Raman data indicates the implantation does not change the a lattice parameter, consistent with the results obtained from XRD.

3.2.3 Piezoelectric Force Microscopy

As explained in section 2.5.4, the amplitude of deflection was plotted against voltage and investigated. We observe a linear increase of the amplitude of deflection with applied voltage between 4 V and 10 V (see Figure 29), which is what is expected for a piezoelectric response. For voltages in the range 0 V to 4 V we can see a slightly non-linear response with a decreasing slope as you approach 0 V. For all samples measured, the 0 V value is approximately 10 pm which is from background vibrations. In order to explain this non-linear response and why linear fitting was done between 4 V and 10 V we take a close look at the distribution of the amplitude and phase.
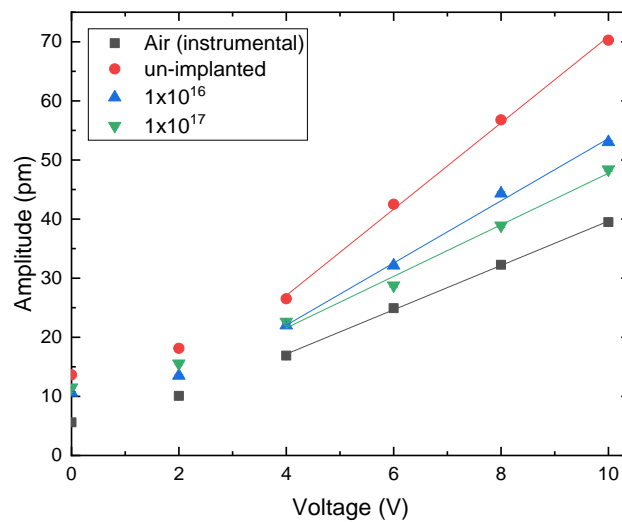

Figure 29: amplitude of deflection (pm) plotted against applied AC voltage for instrumental, un-implanted and two implanted: 1×10^{16} and 1×10^{17} ions/cm^2.

A large number of measurements (1024) of the amplitude and phase were made for each voltage. Attached in the *appendix* is a compilation of the amplitude and phase distributions for each voltage of an example data set for un-implanted AlN. Analysing the amplitude, the data has a Gaussian distribution about a mean value that increases with voltage. For low voltages of 0 V and 2 V the distribution skewed to the right because the amplitude is confined to positive values. For 4 V – 10 V, the mean values, which are larger than 26 pm, are greater than 2x the FWHM of 13 pm, so we do not see the same pile-up effects as those at 0 V and 2 V. Hence, at 0 V and 2 V, the mean value is artificially pushed to slightly higher values, justifying ignoring these voltages for linear fitting. Furthermore, alongside a Gaussian representation, using

Origin, we performed a statistical analysis of the data and find that for 4 V and above the mean and error in the mean, taken as the $RMS/\sqrt{N}$ matches very closely to that determined by a Gaussian fit.

Regarding phase, for 0 V, the phase distribution is a flat, random profile, expected because there is no signal to lock on to. Similar to the amplitude data, the phase distribution has a Gaussian distribution with rapidly decreasing FWHM with voltage. This makes sense because as you increase the applied voltage, the lock-in amplifier has a stronger signal to lock on to. The phase value recorded for each sample is the statistical mean of the 10 V data, as this provides the strongest signal.

To summarise, we have shown the 0 V and 2 V measurements should be ignored in our calculation of A(V). For consistency, it is recommended to include the same range for all samples. The range 4 V – 10 V provides 4 data points for calculating a linear fit, which is adequate, and the slope is denoted as A(V). Due to experimental reasons, we were not able to obtain data for He 1×10^{15} ions/cm^2. Figure 30 presents the fitted amplitude gradient and raw phase data.

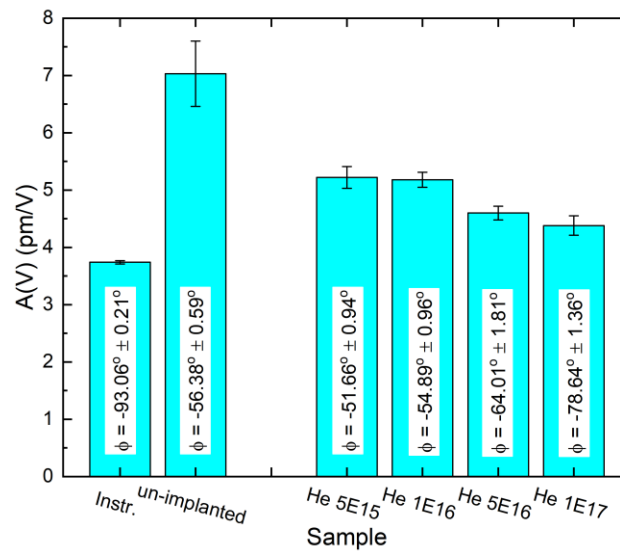Figure 30: bar graph of the slope of the amplitude versus voltage for instrumental and various implanted AlN films. Fluence in ions/cm^2.

A(V) for instrumental is determined by suspending the tip in air to eliminate any electrostatic and piezoelectric responses when in contact with a surface. This is inherent in the system with a value of 3.74 $\pm$ 0.03 pm/V, an error of 0.8 %. We observe that A(V) for the AlN samples is

larger than instrumental, with a general trend of decreasing amplitude with increasing fluence. It is necessary to subtract the background signal. However, this needs to be treated carefully.

The measured signal has an amplitude and a phase and is of the form: $Ae^{i\phi}e^{i\omega t}$, where A the amplitude in pm/V, ϕ is the phase, ω & t are the angular frequency and time respectively. The frequency of the vibration is the same for all samples and is equal to 1 kHz, the frequency of the applied AC voltage. It is suitable to use the instrumental response as the reference phase because it represents the signal absent of any electrostatic and piezoelectric responses. Thus, set the phase of air to 0° and the phases of the AlN samples are simply the difference with respect to air. Thus, when we subtract the instrumental, we now get:

$$\Delta D = A_j e^{i\phi} e^{i\omega t} - A_i e^{i\omega t} = \left[\left(A_j \cos\phi - A_i\right) + iA_j \sin\phi\right]e^{i\omega t} \tag{21}$$

For example, for un-implanted AlN we get:

$$\begin{aligned}\Delta D &= [(7.03\cos(36.68^o) - 3.74) + i7.03\sin(36.68^o)]e^{i\omega t}\\ &= (1.90 + i4.20)e^{i\omega t}\\ &= 4.61e^{i65.68^o}e^{i\omega t}\end{aligned} \tag{22}$$

The largest source of error arises from the variations in amplitude at different locations on the sample surface arising from slight variations in local piezoelectric and electrostatic responses due to an absence of a top electrode. Hence, it is important to take measurements at various locations. In this case, we probed $3 - 5$ locations. The overall A(V) is the average of the multiple runs and error is $2\sigma_{std}/\sqrt{N}$. Figure 31 presents the corrected A(V) for AlN as a function of fluence.
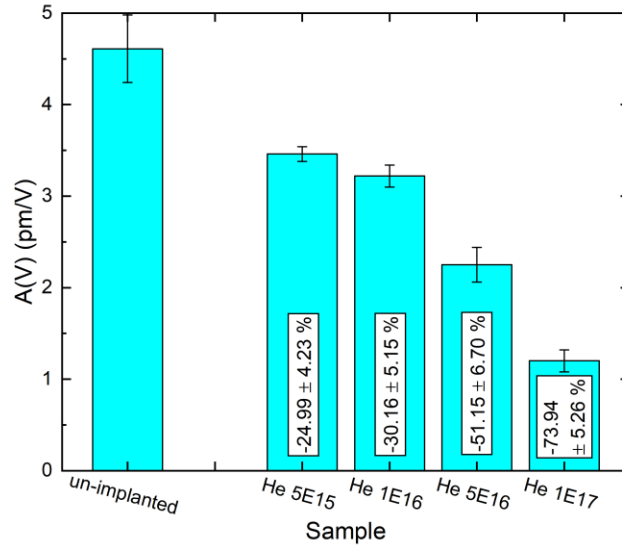
Figure 31: A(V) with instrumental response subtracted. The percentage decrease in amplitudes with respect to un-implanted are written in white. Fluence in ions/cm^2.

With the background subtracted we see that un-implanted AlN has the largest deflection of 4.6 ± 0.4 pm/V. Although this value is a combination of electrostatic and piezoelectric responses, it is in good agreement with d_{33} values in literature of 4.2 ± 0.1 pm/V [19], 4.0 ± 1.8 pm/V [56] and 5.1 ± 0.1 pm/V [11], suggesting our values are reasonable. The trend is A(V) decreases with fluence. The electrostatic response is dependent upon the variability of surface resistivity. Our AlN films have a very high resistivity of ~100 kΩcm, according to the supplier. Therefore, we would not expect such a dramatic change with the He implantation. Thus, the relative changes can be attributed to a reduction in piezoelectric response.

3.3 Conclusions

In this chapter we have studied the effect of He implantation on the structural, vibrational and piezoelectric properties of AlN thin films. One of the hypotheses of the proposed study was that He implantation would enhance the uniaxial strain along the c-axis. XRD results support this hypothesis, with the strain increasing by 1% for a fluence of 1×10^{17} ions/cm^2. Interestingly enough we do not observe a change in the a-axis, which is attributed to the growth direction of the films and implantation procedure being along the c-axis. It is worth pointing out that XRD suggests the formation of a second phase at fluences above 1×10^{16} ions/cm^2 which we attribute to the formation of He bubbles. TEM would be an appropriate characterisation technique to verify this. The generation of a dual-strained region could mark an amorphization threshold in

the vicinity of 1 x 10^{16} and 5 x 10^{16} ions/cm^2. We find evidence of a reduction in the piezoelectric response with increasing fluence that can be attributed to the introduction of disorder in the lattice. This is supported by Raman spectroscopy with a reduction in intensity and broadening of the E_2(high) mode indicating fewer particles coherently Raman scattering, and additionally, a reduction in the phonon mean free path.

Chapter 4 AlN Implanted with Sc

4.1 Implantation Summary

30 keV Sc^+ ions were implanted into 100 nm thin AlN films on a Si <111> substrate at various fluences. The impact was at normal incidence and uniform across the surface. At the time, the highest electric field we could generate using the implanter at GNS was 30 kV. The desired fluence and measured fluence (from RBS) are summarised in the table below. The same ion beam implanter and geometry as that to implant the He^+ ions was used. More details on the system can be found in section 2.4.

Table 5: desired fluence, DTRIM retained fluence and RBS measured fluence (ions/cm^2) for Sc implantation.

Desired fluence	DTRIM retained fluence	Measured fluence
1.00×10^{15}	1.00×10^{15}	1.11×10^{15}
5.00×10^{15}	5.00×10^{15}	5.48×10^{15}
1.00×10^{16}	1.00×10^{16}	1.43×10^{16}
5.00×10^{16}	4.73×10^{16}	6.52×10^{16}
1.00×10^{17}	0.79×10^{17}	1.15×10^{17}

4.1.1 Dynamic Transport and Range of Ions in Matter

DTRIM simulations were performed to obtain the implantation profile and other useful parameters such as the sputtering yield, mean projected range and Al/N ratio.
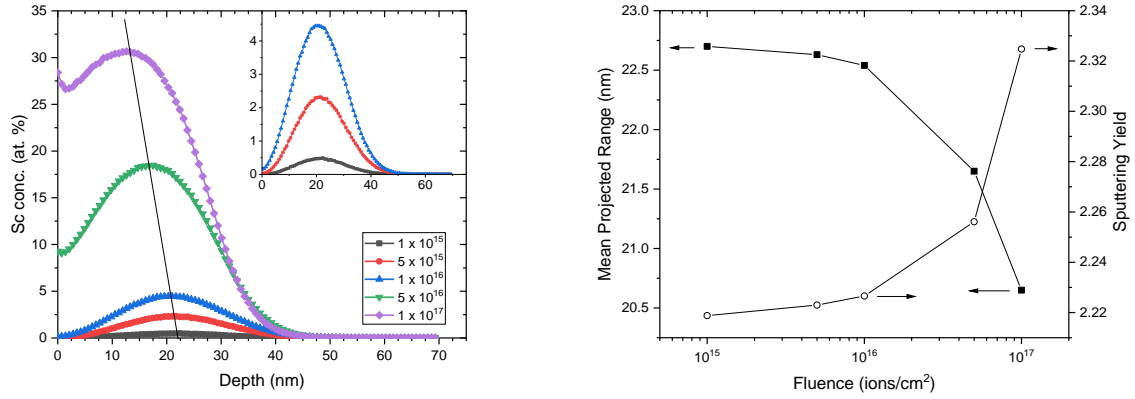

Figure 32: (left) DTRIM simulations of Sc^+ implanted into AlN with energy 30 keV at normal incidence. The inset is a magnification of the fluences up to 1×10^{16} ions/cm². (right) mean projected range and sputtering yield as a function of fluence (ions/cm²).

At low fluences (1×10^{15} to 1×10^{16} ions/cm²) we observe a Gaussian distribution of projected Sc atoms inside the AlN lattice confined to a maximum penetration of 50 nm. The mean projected range is 22.7 nm with a FWHM of 20 nm (1×10^{15} ions/cm²). At higher fluences we see a build-up of Sc on the surface. This is coupled with the fact that the mean projected range becomes shallower with fluence, as indicated in Figure 32. These effects are attributed to the re-sputtering of Sc from increasing Sc-Sc interactions. Additionally, the sputtering yield increases from 2.22 to 2.32 for fluences of 1×10^{15} and 1×10^{17} ions/cm² which is also due to increasing Sc-Sc interactions.

The DTRIM simulations predict that for a fluence of 1×10^{15} ions/cm² the peak atomic concentration of Sc is 0.5% (~20 nm depth), which corresponds to approximately 1 implanted Sc atom per 200 Al atoms (or N atoms) or 1 Sc atom per 6 x 6 x 6 Al atoms (or N atoms) inside the lattice. For a fluence of 1×10^{17} ions/cm² the peak concentration is 30%, corresponding to 1 Sc atoms per cube of 1.5 x 1.5 x 1.5 Al atoms, significantly more.

Additionally, using DTRIM we computed the Al/N ratio as a function of depth (see Figure 33). Immediately on the surface, there is a striking abundance of Al compared to N, which is related

to sputtering effects. In DTRIM, an atom is sputtered out if the energy transferred to it during a collision is greater than the surface binding energy and the resulting motion is towards the surface [35]. From table bases [57], DTRIM determined the surface binding energy of N (3.00 eV) is lower than Al (3.36 eV) resulting in it being easier to sputter N compared to Al. At a depth of 10 to 30 nm the Al/N ratio is also greater than 1, predominantly for fluences of 5 x 10^{16} ions/cm^2 and 1 x 10^{17} ions/cm^2. This can be attributed to the heavy Sc atoms displacing N atoms further away from their original sites than Al, from sputtering and burying the displaced atoms further down into the lattice. The latter can be observed as there is a slight net of N around 40 nm deep.
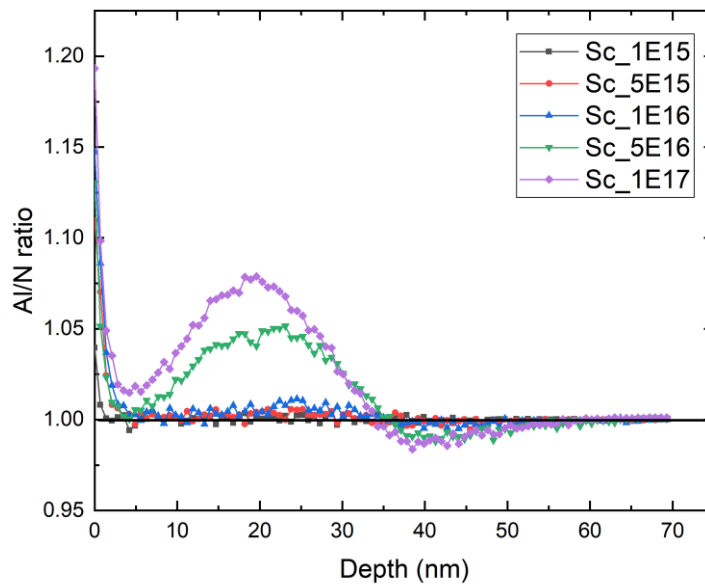

Figure 33: Al to N ratio plotted as a function of depth for the implantation.

4.2 Experimental Results and Analysis

4.2.1 Rutherford Back-Scattering

Rutherford back-scattering was performed to experimentally verify the amount of Sc implanted into the films and the composition of other elements. 2 MeV He$^+$ were fired at normal incidence on the sample and the back-scattered ions were measured at 165° with a surface barrier detector. For more information on the experimental details, please refer to [58]. For more information on RBS, please refer to [59].

We detect peaks corresponding to N and Al buried inside a broad substrate peak and, additionally, a Sc peak at higher energies. These assignments were verified using RUMP simulation [1]. The RBS data for a fluence of 1 x 10^{17} ions/cm^2 with RUMP simulation and RBS Sc peaks for all fluences are presented in Figure 34.
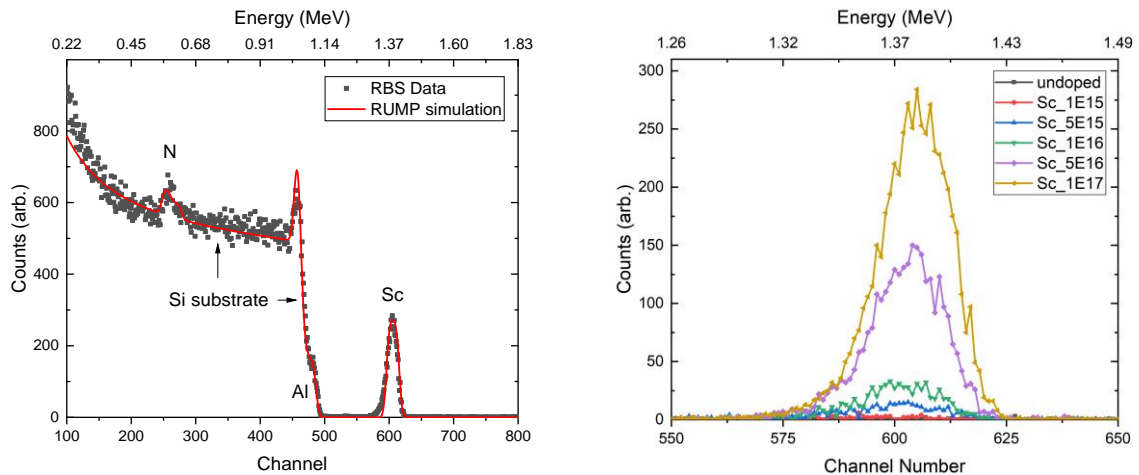

Figure 34: (left) RBS data of AlN implanted with Sc at a fluence of 1 x 10^{17} ions/cm^2 with RUMP simulation illustrating N, Al and Sc peaks; (right) close-up of Sc peak for all implanted samples.

The right edge of the Al peak just catches the onset of the Si substrate which is why it is sliced in half. The Sc peaks at an energy of 1.38 MeV verify the presence of Sc in the film. The integrated intensity of this peak confirms the correct ratios of fluence in Figure 35. Additionally, using RUMP simulations performed by Peter Murmu at GNS, the actual fluence

---

[1] For more information on RUMP software please refer to http://www.genplot.com/doc/rump.htm

was calculated (see Figure 36). There is a slight over-fluence for each implantation, but the overall ratio is close 1:1, indicating a successful implantation.

Interestingly, the Sc peak is slightly asymmetric; most noticeable for a fluence of 1 x 10^{17} ions/cm^2. The larger gradient of the peak on the higher energy side is indicative of a sharper onset of Sc in the film. Indeed, this can be physically explained by the step transition from no Sc above the surface of the film to a presence of Sc on the surface. There is a continuous transition of Sc to no Sc inside the film, hence a smaller gradient on the lower energy side.
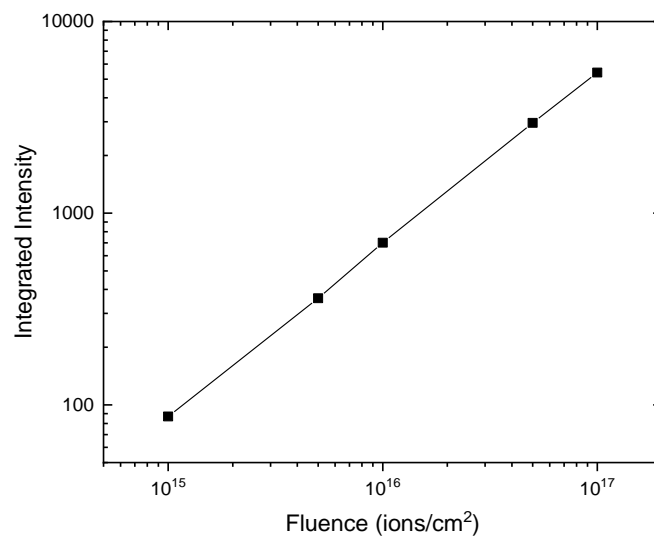
Figure 35: total no. of counts (integrated intensity) for Sc RBS peak for each fluence.
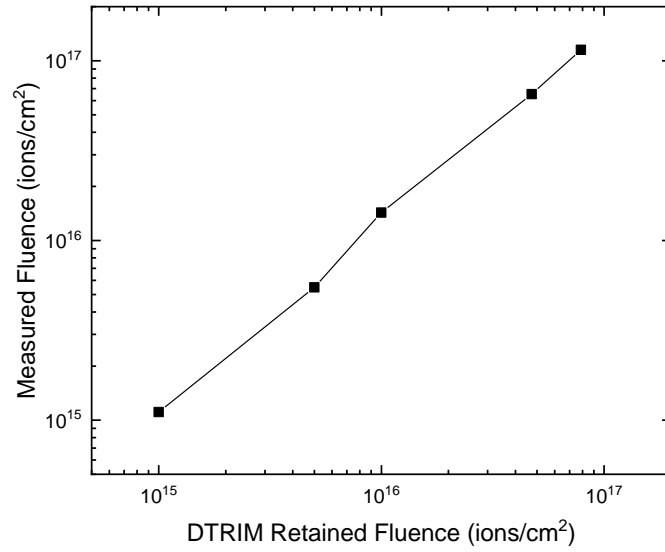
Figure 36: measured fluence plotted against DTRIM retained fluence.

4.2.2 Current-Voltage Measurements

Next, we shall qualitatively take a look at surface electrical characterisation of the chips. A 2pt probe was utilised to characterise the surface resistance of the Sc implanted chips. A current was supplied from -50 μA to +50 μA and the voltage difference was measured using an electrometer.
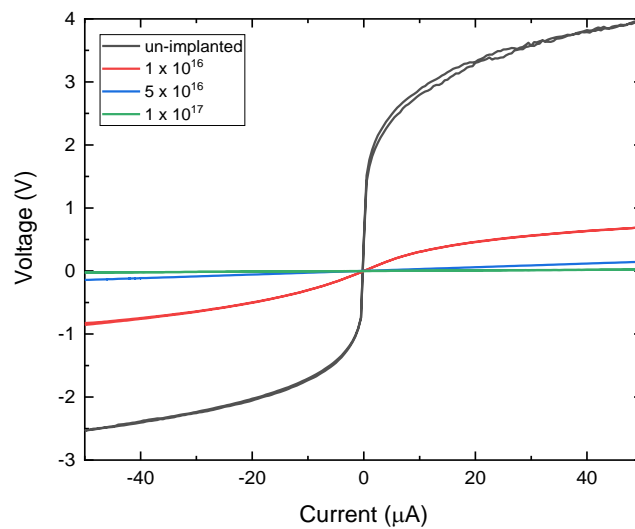
Figure 37: IV curve for AlN implanted with Sc. Fluence in ions/cm^2.

We observe a highly non-linear response, suggesting non-ohmic behaviour for un-implanted which is characteristic of the semi-conducting film. We may also be picking up the conductive Si substrate underneath. The "flattening" of the curve is indicative of increasing conductivity which is due to the addition of Sc into the film. From a fluence of 1×10^{16} to 5×10^{16} ions/cm^2, there is a clear transition from non-linear to linear, therefore non-ohmic to ohmic which is consistent with the DTRIM interpretation of a Sc build-up on the surface. Also, you can physically see a colour transition from blue to grey on the samples (Figure 9).

4.2.3 X-Ray Diffraction

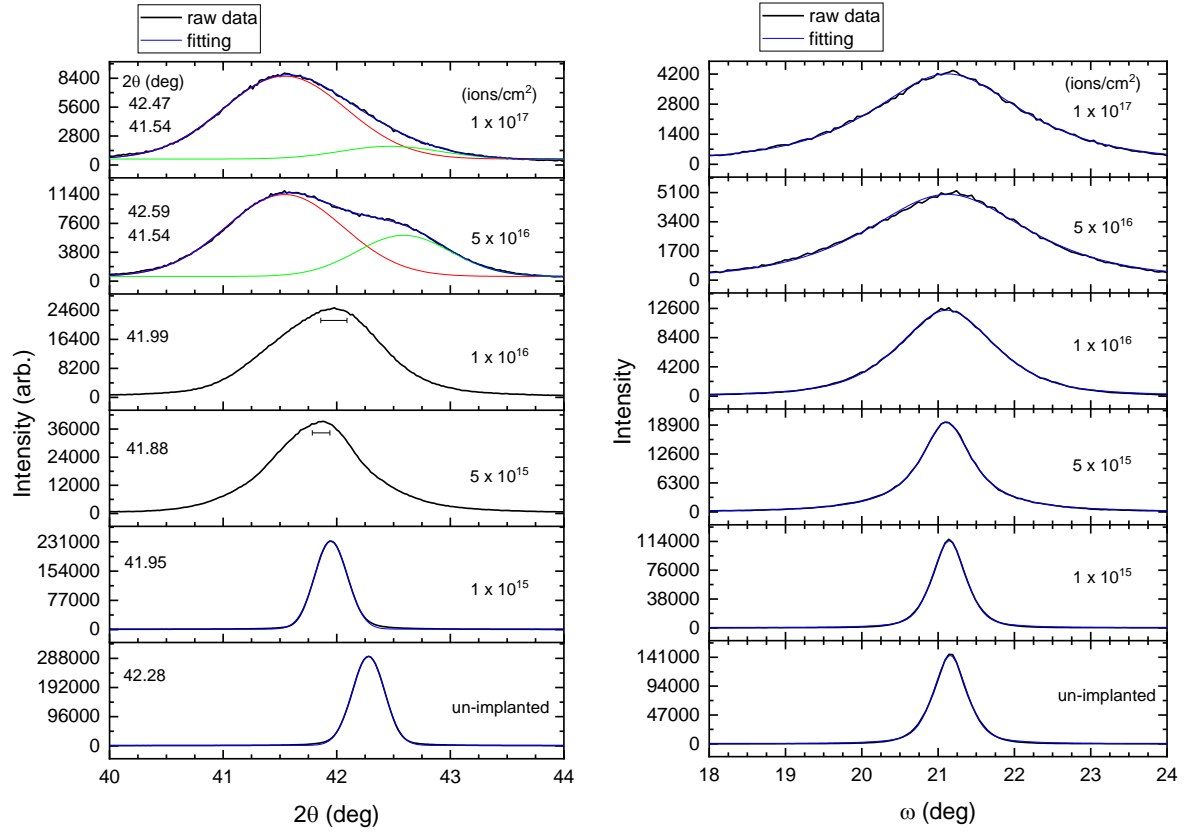Figure 38: out-of-plane $2\theta - \omega$ scan and rocking curve of Sc implanted AlN, showing peaks for (002) planes. Black line is raw data and blue line is fitting. The red and green curves are the individual Gaussian fits for the double peak.

The $2\theta - \omega$ and rocking curve data for (002) and (100) planes are presented in Figure 38 and Figure 40, respectively. Similar to the AlN implanted with He, the $2\theta_{002}$ are fit with Gaussian function(s) and the rocking curve with pseudo-Voigt. The Sc implantation produces strain inside the lattice that is tensile, shown by the $2\theta_{002}$ shifting to lower values with increasing fluence. At intermediate fluences (5 x 10^{15} and 1 x 10^{16} ions/cm^2) the peak becomes asymmetric and broadens, likely due to an increase in Sc concentration causing inhomogeneous strain.

At high fluences (5 x 10^{16} and 1 x 10^{17} ions/cm^2) there is a bimodal distribution of peaks which are fit extremely well with double Gaussians. The main peak at 41.54^{o} is at lower values to the other fluences, so is a result of the tensile strain. The emergent second peak is at a higher angle of 42.50^{o}, indicating compressive strain, which could be from a thin surface Sc layer. To support this claim, the physical appearance of the samples becomes grey (Figure 9) and DTRIM models a build-up of Sc (Figure 32) in the first few nm. From theoretical predictions, Sc is

expected to produce two peaks in the vicinity of the 2θ observed of 41.74° $(10\bar{1}1)$ and 40.46° (0002) [2]. Although these theoretical values are lower than what are observed, at thin surface layer of Sc is likely to be strained by the film underneath and so it is reasonable to obtain a higher 2θ than that predicted. TEM would be a suitable characterisation technique to complement XRD to verify he nature of the crystal structure post-implantation and should be performed in future work related to this project. It has been reported by Williams *et al.* that clusters of metal precipitate in the top layer of the film, followed by a region immediately below with a lower concentration, have been observed for low energy (10 keV) implantation of Ni^+ into SiO_2 at 4×10^{16} ions/cm^2 [60]. It is worth pointing out that the $2\theta_{002}$ peak for *wurtzite*-$Sc_xAl_{1-x}N$ alloys has been reported at similar values for AlN for various concentrations, *x = 0.06* [61, 62] and *0 < x < 0.30* [10], therefore it is also possible that at the high fluences, the concentration of Sc may be high enough for alloying to occur, however TEM is needed to verify this for our films.
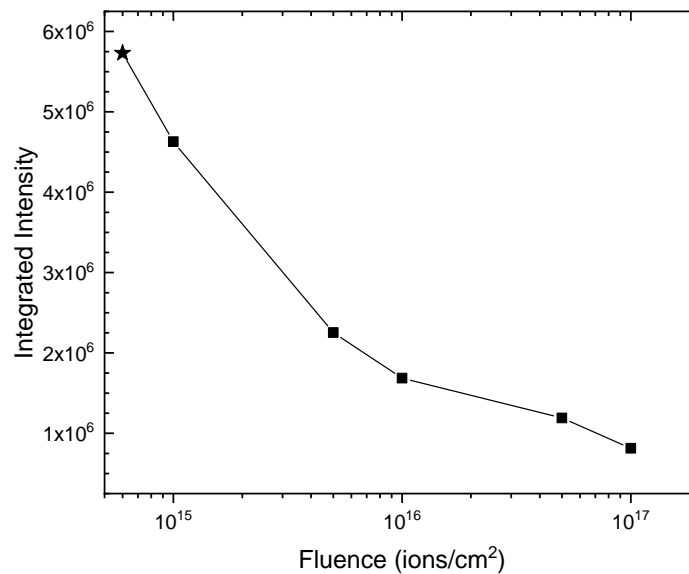

Figure 39: integrated Intensity of $2\theta_{002}$ for AlN films implanted with Sc as a function of fluence. Note: the star symbol represents un-implanted AlN.

---

[2] The theoretical predictions are modelled for hexagonal close-packed Sc from the website www.materialsproject.org. Please visit the website for more details.

As represented in Figure 39, the integrated intensity of $2\theta_{002}$ decreases consistently with fluence, indicating the heavy ion implantation is damaging the lattice, which increases with fluence.

The (002) rocking curves in Figure 38 show increasing FWHM with fluence from 0.52° (un-implanted) to a maximum of 2.56° (5 x 10^{16} ions/cm²), a fivefold increase, indicating the heavy Sc ions cause significant tilting of grains about the *c*-axis. The increased tilting could be from destruction of crystal grains, although TEM is needed to verify this.
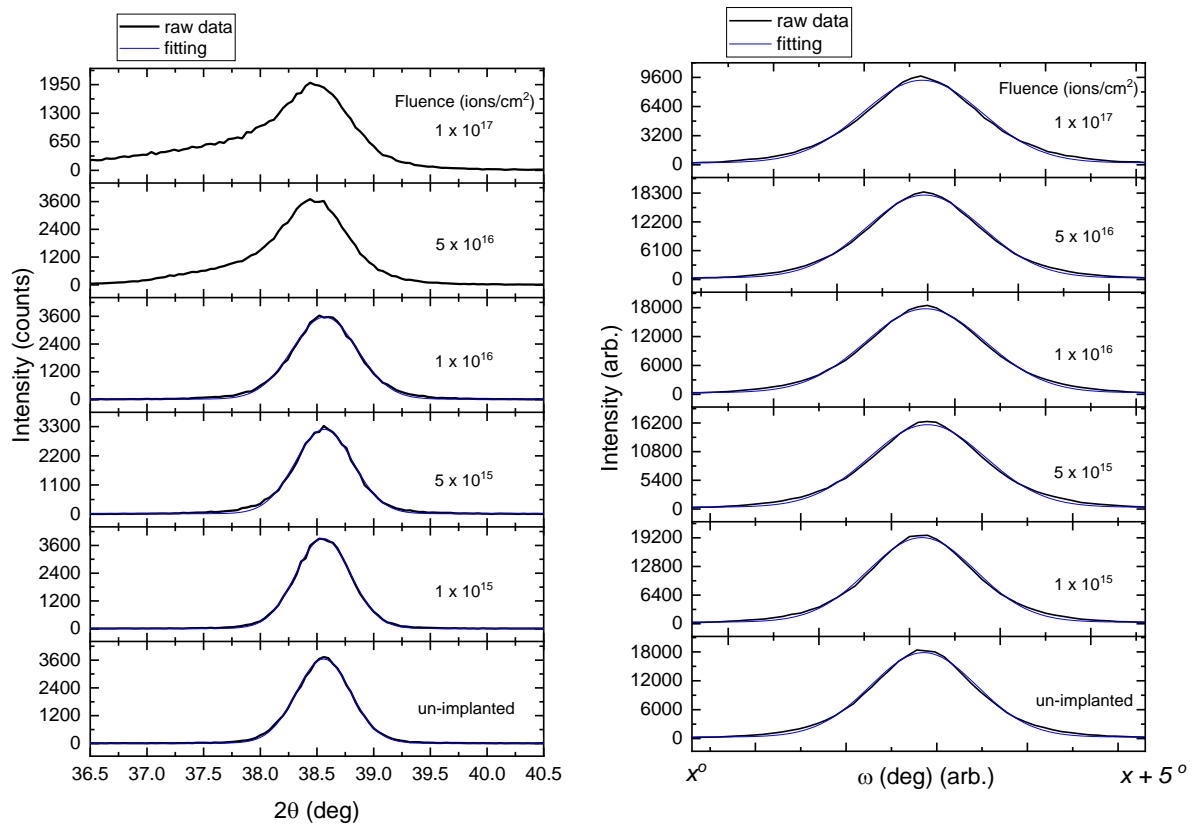
Figure 40: in-plane $2\theta_\chi - \phi$ scan (left) and rocking curve (right) of Sc implanted AlN, showing peaks for (100) planes.

The changes to the lattice in the basal plane are not as significant as that in the *c*-axis. Up to a fluence of 1 x 10^{16} ions/cm², the $2\theta_{100}$ peaks have a Gaussian shape centred around 38.56° with a FWHM of 0.57°. At higher fluences the peaks become asymmetric to lower values. This suggests inhomogeneous expansion in the basal plane, most likely due to damage imposed by the Sc implantation.

The rocking curve for (100) shows little to no variation in FWHM, whereas there is broadening of a factor of 5 for (002). This is likely due to the film being more susceptible along the *c*-axis than the *a*-axis as a result of the *c*-axis growth direction and implantation; the *a*-axis is locked to the substrate. Lorenz *et al.* report *w*-GaN being less susceptible to radiation damage along the *a*-axis than the *c*-axis by a factor of 4 [14].

4.2.4   Raman Spectroscopy

Raman spectroscopy was performed on all AlN samples implanted with Sc, including un-
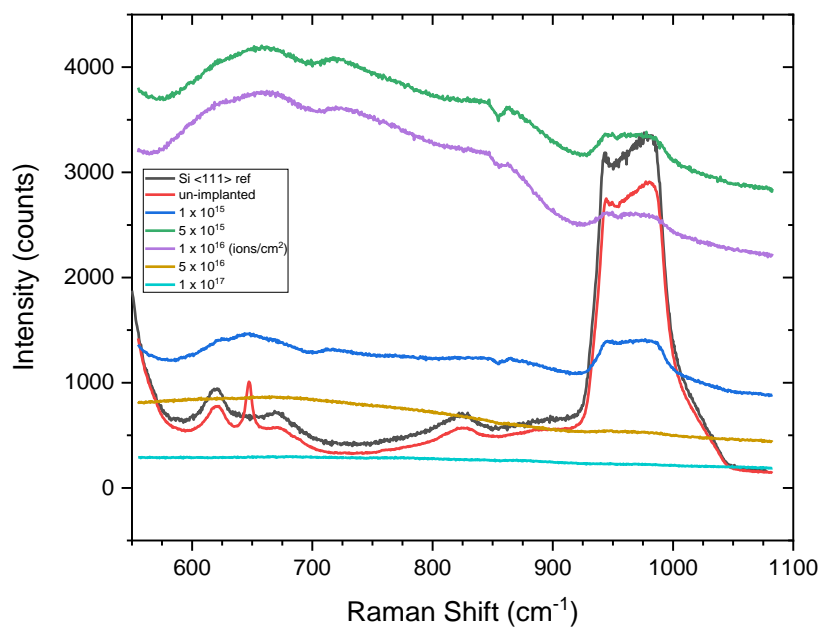
Figure 41: Raman spectra of AlN implanted with Sc at various fluences (ions/cm^2).

implanted and Si(111) substrate as a reference. To keep the same conditions as the He implanted samples, the same parameters were employed, namely a laser wavelength of 514.5 nm at 5 mW, back-scattering geometry, x100 objective, 1800 lines/mm grating and 60 s acquisition averaged multiple times. We would like to analyse the effects of the Sc implantation on the Raman spectrum of AlN.

The acquired data is shown in Figure 41. Scandium is a heavy ion and the DTRIM simulations suggest that the implantation is near-surface; only the top 50 nm is implanted, creating a much larger concentration than if the Sc was dispersed throughout the entire volume, such as the case for the He implantation. Moreover, Sc is not inert and has the potential to substitute Al to form ScN, unlike He which is inert and sits in interstitial sites in the lattice. Therefore, we would

expect the Raman spectra to be more significantly affected than with the He ions. For the lowest fluence of 1 x 10^{15} ions/cm^2, DTRIM suggests the maximum concentration of Sc is 0.5 % (relative atom number). Although a more rigorous approach is ideal, we can estimate the average spacing between each Sc atom, as follows:

The volume concentration is 0.005 Sc atoms per Al (or N) atom, which, if we assume to be the same in the *x*, *y*, and *z* directions, leads to $\sqrt[3]{0.005} = 0.17 \ (2dp)$ or about 1 Sc per 6 Al atoms (or N atoms) along each direction. In the basal plane, the lattice parameter is 3.1 Å, meaning that each Sc atom is approximately 18 Å apart or 1 Sc for every 3 unit cells. If each Sc atom is a site for the termination of a phonon then this is expected to cause broadening of the Raman peaks, by reducing the phonon mean free path.
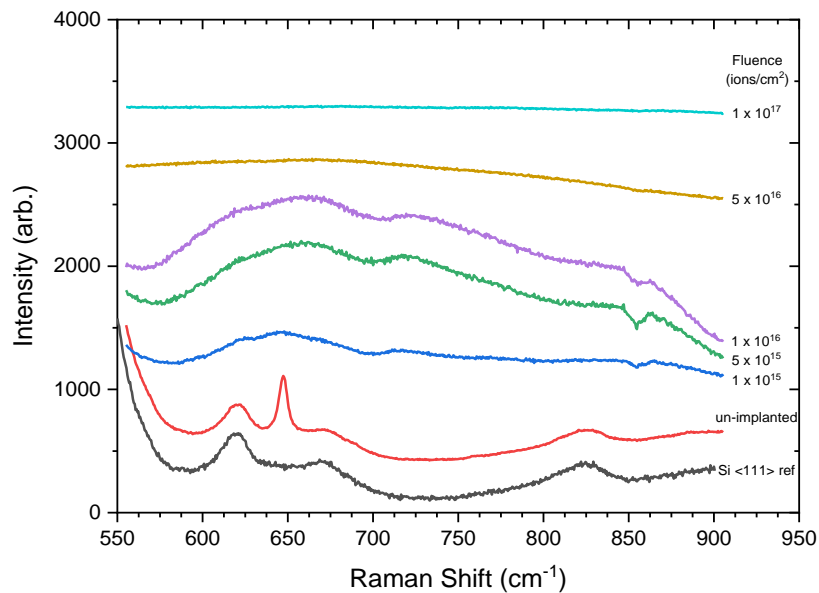
Figure 42: Raman spectra of Si (111) and AlN implanted with Sc at various fluences.

In Figure 42, we can clearly see the same Si modes and E_2(high) peak as in Figure 28, demonstrating reproducibility. The E_2(high) is at 647.5 ± 1.2 cm^{-1}, which is about 1.5 cm^{-1} lower than the un-implanted AlN presented in Figure 28, which is probably due to the fact these AlN are on different wafers, so some strain differences from the substrate are expected.

The most striking observation is that all peaks become severely attenuated and unresolvable even for the lowest implanted fluence (1 x 10^{15} ions/cm^2). The severe attenuation and broadening of the E_2(high) is likely to be from the heavy Sc atoms serving as termination points for phonons. Even the lowest fluence is sufficient enough to make the E_2(high) mode almost unresolvable. At fluences higher than 1 x 10^{15} ions/cm^2 the mode is unresolvable. Additionally,

the flat-line of the 5×10^{16} and 1×10^{17} ions/cm^2 implanted samples is in agreement with the interpretation of a surface Sc layer forming. This is because a surface Sc metallic layer will act as a mirror and reflect the incoming laser beam instead of transmitting it, quenching all Raman signals.

4.2.5 Piezoelectric Force Microscopy

To investigate the electromechanical properties of the AlN thin films, which would include the piezoelectric charge coefficient in the c-axis (d_{33}), PFM was performed on the AlN implanted with Sc with the same experimental conditions as with He. For reproducibility and reliability, measurements were done on $3 – 5$ different locations on the surface of each sample. Furthermore, the procedure was repeated over several days and a new tip used each time. Additionally, the samples were measured in a random order to eliminate observing any drift effects as trends. The treatment of the collected data to obtain the amplitude of deflection as a function of voltage A(V) is explained in section 3.2.3. Figure 43 presents the A(V) for AlN implanted with Sc at various fluences for multiple runs.

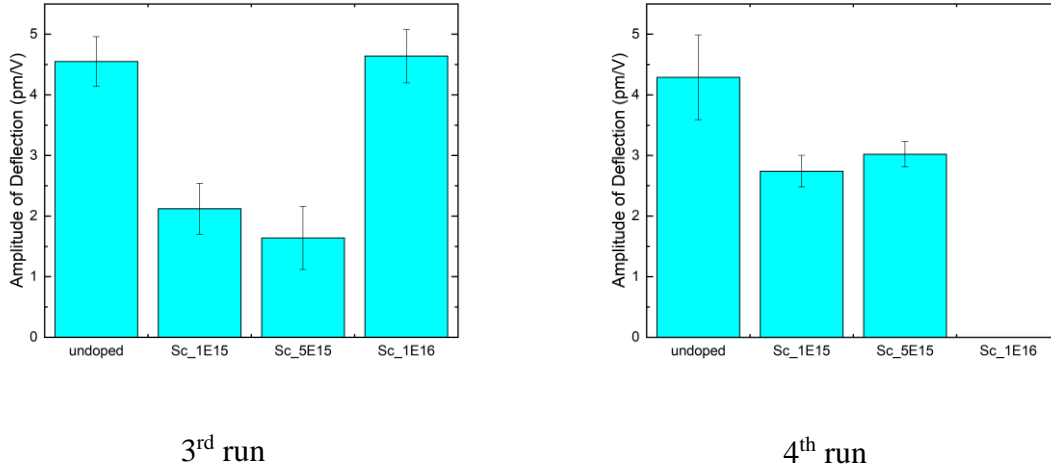1$^\text{st}$ run   2$^\text{nd}$ run

<div align="center">3rd run   4th run</div>
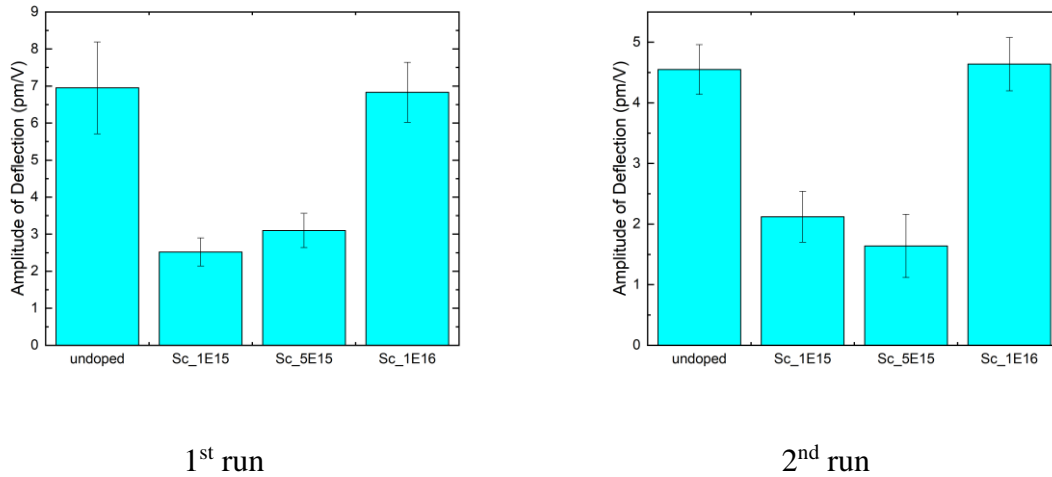
Figure 43: PFM data of AlN implanted with Sc. A(V) in pm/V on *y*-axis plotted against each implanted sample on *x*-axis, with sample code shown: implanted ion, then fluence in ions/cm^2. Uncertainties are to 2 standard errors in the mean.

We were unable to measure the high fluences of 5 x 10^{16} and 1 x 10^{17} ions/cm^2 due to a conductive bridge forming between the Si substrate and the surface of the film (likely due to a metallic Sc surface layer). For experimental reasons, we were unable to collect data for a fluence of 1 x 10^{16} ions/cm^2 in the 4th run.

The deflections for the 1st run are about 2 pm/V larger than the others, which is attributed to variations between tips. However, all data is in the proximity to that expected for AlN which has a reported d_{33} of 5.1 ± 0.1 pm/V [11].

There is a decrease in the deflection amplitude by a factor of ~2 for 1 x 10^{15} and 5 x 10^{15} ions/cm^2 compared to un-implanted. The deflection of 1 x 10^{16} ions/cm^2 is consistently at the same level as un-implanted within uncertainties. Without identical top electrodes for all samples, it is difficult to discern whether this variation is purely electrostatic, piezoelectric or a combination of the two. However, we shall try our best to relate with the other characterisations performed.

The Raman data informs us that the severe attenuation and broadening of the E$_2$(high) Raman peak (Figure 42) even at the lowest fluence of 1 x 10^{15} ions/cm^2, suggests the implanted Sc significantly reduces the phonon mean free path, introducing disorder in the lattice. Therefore, a possible interpretation is that for the low fluences of 1 x 10^{15} and 5 x 10^{15} ions/cm^2, lattice disorder reduces the piezoelectric charge coefficient and is responsible for the relative decrease

in A(V). Regarding 1×10^{16} ions/cm^2, we know from the IV curve (Figure 37) the surface conductivity of the film at this fluence is greatly enhanced. Therefore, it may be that a thin Sc layer in the first few nm of the film is enhancing the electric field for the bulk AlN by acting as an electrode, enhancing the overall deflection. It has been reported that a top electrode increases the measured piezoelectricity of AlN thin films [49].

4.3   Conclusions

In this chapter we have investigated the effects of Sc implantation on the structural, vibrational and piezoelectric properties of AlN thin films. RBS analysis was used to determine the profile and concentration of Sc in the AlN film after implantation. The results show a good agreement with initial DTRIM, with the Sc implantation confined to within the first 50 nm of the film, leading to a conductive top layer within the AlN film for fluences of 5×10^{16} and 1×10^{17} ions/cm^2 as is confirmed by the current-voltage curves.

XRD analysis reveals that Sc produces expansive c-axis strain that increases with fluence with minor changes in the basal plane. For intermediate fluences of 5×10^{15} and 1×10^{16} ions/cm^2, the c-axis strain becomes more inhomogeneous, suggesting damage imposed on the lattice. For higher fluences there is additionally a second region of compressive strain that, with the support of the IV measurements, XRD and Raman spectroscopy, is likely to be from a surface layer of Sc. It is difficult to determine whether there are alloying effects in the film without TEM.

Initial PFM measurements show a decrease in the amplitude of deflection for 1×10^{15} and 5×10^{15} ions/cm^2, that could be due to disorder introduced by the Sc implantation. This is supported by Raman spectroscopy measurements which show significant broadening and reduction in intensity of the E$_2$(high) Raman mode. Perhaps what is more interesting is the electromechanical response increases back to the same level as un-implanted for 1×10^{16} ions/cm^2 suggesting an enhancement of the electric field by the Sc. Clearly it would be central to focus on higher fluences as part of the future work. Unfortunately, within the limited time allowed by the thesis we have not been able to measure them. I also propose using another tool to measure the piezoelectric response such as a network analyser, which would allow to measure the acoustic properties directly via the fabrication of a SAW/BAW device.

Chapter 5 Summary and Outlook

5.1 Thesis Overview

In summary, AlN thin films were implanted with He (light) and Sc (heavy) ions and investigated for their structural, vibrational and piezoelectric properties using experimental techniques such as Raman spectroscopy, XRD and PFM. I was interested to investigate whether we could generate strain or form alloys with the different types of ions and if this could increase the piezoelectricity of AlN thin film. Using XRD, we can confirm that both implanted ions created uniaxial strain along the *c*-axis that is expansive, with minimal changes to the *a*-axis. An interesting similarity is that both types of ions demonstrate the formation of dual-strained regions above a fluence of 1 x 10^{16} ions/cm^2. Although TEM is needed to verify the crystal structure, a possible interpretation is that the secondary phase is from He bubbles for the He implantation and either nano-crystalline Sc or ScAlN alloying effects for the Sc implantation.

The reductions in measured deflections from PFM for both ions are attributed to disorder introduced in the lattice by the implantation. This is supported by Raman spectroscopy where the E_2(high) Raman mode broadens and reduces in intensity with fluence, indicating a decrease in the phonon mean free path. This suggests the piezoelectric response is more strongly influenced by changes in vibrational properties than strain-induced effects.

5.2 Future Direction

I believe this thesis provides a basis for future work to be pursued in the following ways:

- A key result of this thesis is that XRD suggests changes in the crystal structure of the AlN thin film from the implantation. To provide further detail on the nature of the crystal structure, TEM is a useful technique. Using TEM we should be able to verify whether the secondary phases are from He bubbles and nano-crystalline Sc. TEM will also tell us where in the lattice the secondary phase forms.

- Use a network analyser to provide a second reference for piezoelectric measurements. A network analyser is used to measure the filter characteristics for SAW and BAW. One of the pieces of information obtained is the electromechanical coupling coefficient from which the piezoelectric charge coefficient can be determined. This avoids any issues with electrostatic interactions.

- Perform a staggered implantation for low fluences creating a box-like profile. This will ensure a more uniform distribution of implanted ions through the whole lattice rather than implanting at one energy. It may be the case that a box-like implantation combined with annealing to recover damage may be the best combination, so is an avenue to be interested in.

Appendix

Attached in the following pages is the data for PFM measurements performed on un-implanted AlN. The amplitude and phase data for each voltage are presented with a Gaussian fit and statistical average.

0V
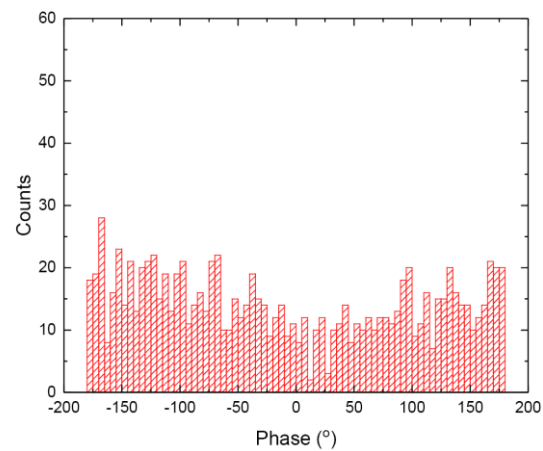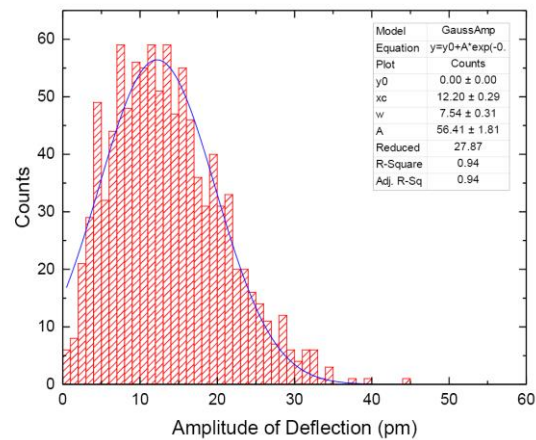
<u>Data on mean</u>

<u>Amplitude</u>
Gauss fit: 12.20 ± 0.29 pm
stats: 13.66 ± 0.22 pm
$\sigma_{std\ dev}/\sqrt{N} = 0.22$ pm

<u>Phase</u>
N/A
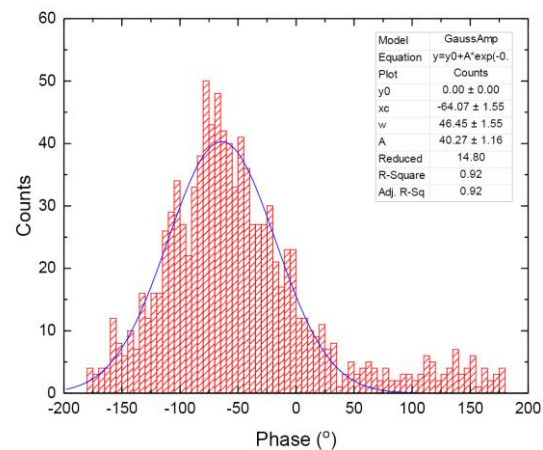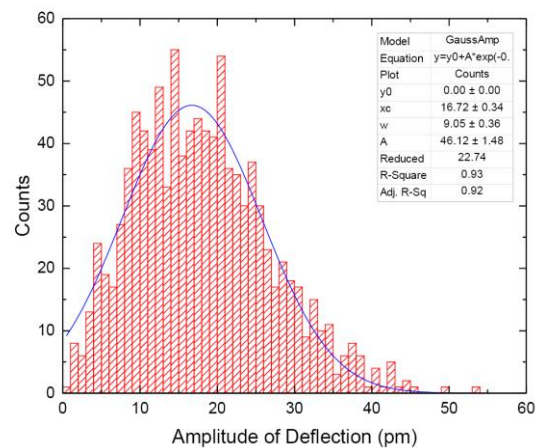
2V

<u>Data on mean</u>

<u>Amplitude</u>
Gauss fit: 16.72 ± 0.34 pm
stats: 18.12 ± 0.27 pm
$\sigma_{std\ dev}/\sqrt{N} = 0.27$ pm

<u>Phase</u>
Gauss fit: $-64.07º \pm 1.55º$
stats: $-47.81º \pm 2.13º$
$\sigma_{std\ dev}/\sqrt{N} = 2.13º$
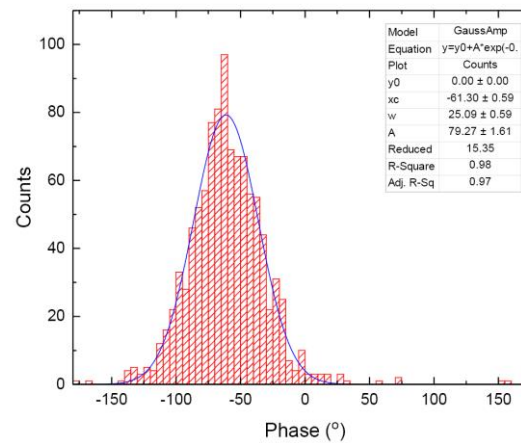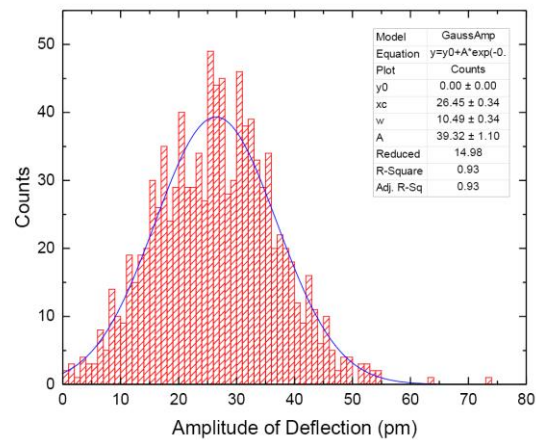
		4V

Data on mean

Amplitude
Gauss fit: 26.45 ± 0.34 pm
stats: 26.52 ± 0.32 pm
$\sigma_{std\ dev}/\sqrt{N}$ = 0.32 pm

Phase
Gauss fit: -61.30º ± 0.59º
stats: -60.14º ± 0.96º
$\sigma_{std\ dev}/\sqrt{N}$ = 0.96º
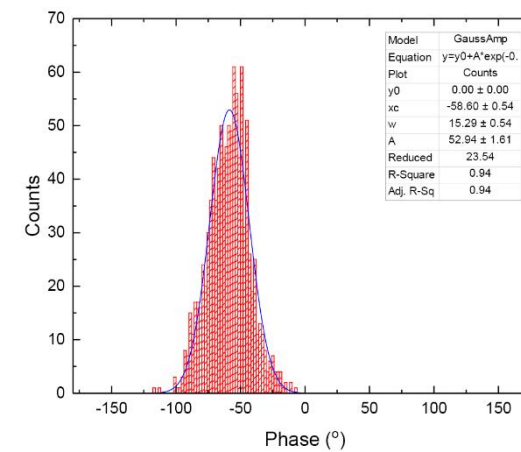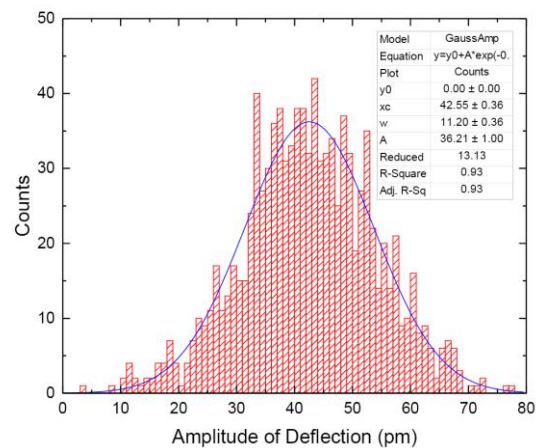
6V

Data on mean

Amplitude
Gauss fit: 42.55 ± 0.36 pm
stats: 42.49 ± 0.36 pm
$\sigma_{std\ dev}/\sqrt{N}$ = 0.36 pm

Phase
Gauss fit: -58.60º ± 0.54º
stats: -59.15º ± 0.49º
$\sigma_{std\ dev}/\sqrt{N}$ = 0.49º

Model	GaussAmp
Equation	y=y0+A*exp(-0.
Plot	Counts
y0	0.00 ± 0.00
xc	56.23 ± 0.33
w	11.16 ± 0.33
A	36.51 ± 0.92
Reduced	11.26
R-Square	0.94
Adj. R-Sq	0.94

x-axis: Amplitude of Deflection (pm), y-axis: Counts

Model	GaussAmp
Equation	y=y0+A*exp(-0.
Plot	Counts
y0	0.00 ± 0.00
xc	-56.67 ± 0.29
w	11.11 ± 0.29
A	73.55 ± 1.64
Reduced	17.71
R-Square	0.97
Adj. R-Sq	0.97

x-axis: Phase (°), y-axis: Counts
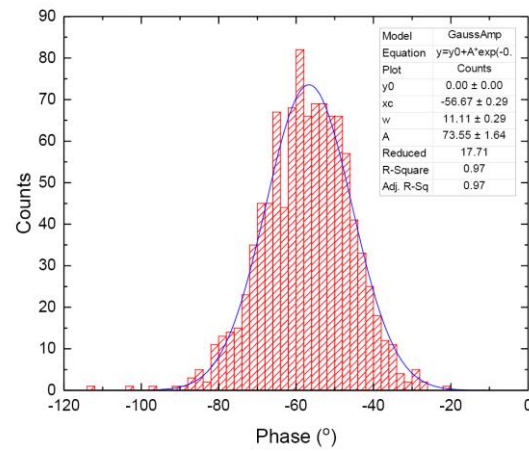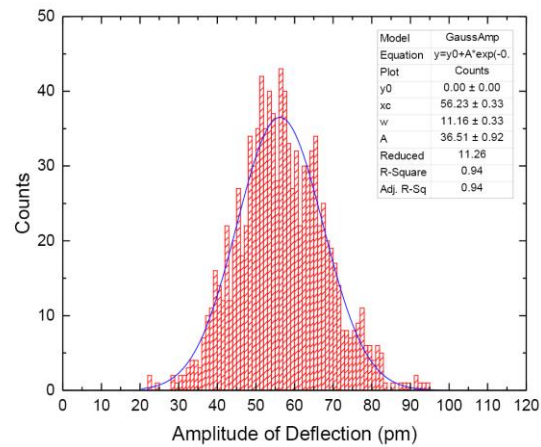
<u>8V</u>

<u>Data on mean</u>

<u>Amplitude</u>
Gauss fit: 56.23 ± 0.33 pm
stats: 56.77 ± 0.35 pm
$\sigma_{std\,dev}/\sqrt{N} = 0.35$ pm

<u>Phase</u>
Gauss fit: -56.67º ± 0.29º
stats: -57.21º ± 0.35º
$\sigma_{std\,dev}/\sqrt{N} = 0.35$º

Model	GaussAmp
Equation	y=y0+A*exp(-0.
Plot	Counts
y0	0.00 ± 0.00
xc	70.66 ± 0.40
w	11.75 ± 0.40
A	34.92 ± 1.02
Reduced	14.43
R-Square	0.92
Adj. R-Sq	0.91

x-axis: Amplitude of Deflection (pm), y-axis: Counts

Model	GaussAmp
Equation	y=y0+A*exp(-0.
Plot	Counts
y0	0.00 ± 0.00
xc	-55.88 ± 0.20
w	9.16 ± 0.20
A	89.51 ± 1.70
Reduced	15.68
R-Square	0.99
Adj. R-Sq	0.99

x-axis: Phase (°), y-axis: Counts
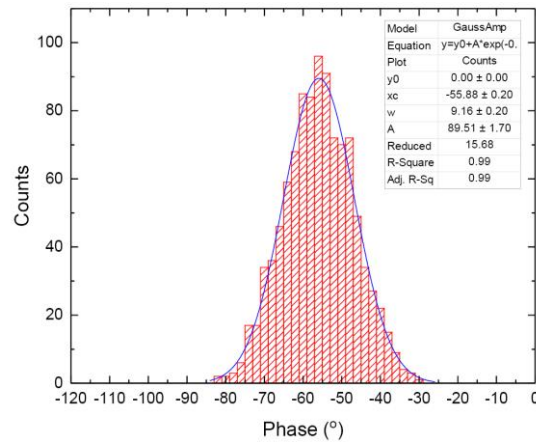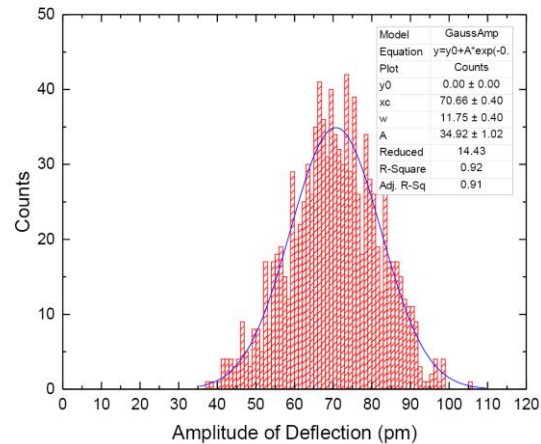
<u>10V</u>

<u>Data on mean</u>

<u>Amplitude</u>
Gauss fit: 70.66 ± 0.40 pm
stats: 70.27 ± 0.36 pm
$\sigma_{std\,dev}/\sqrt{N} = 0.36$ pm

<u>Phase</u>
Gauss fit: -55.88º ± 0.20º
stats: -55.87º ± 0.28º
$\sigma_{std\,dev}/\sqrt{N} = 0.28$º

References

1. Osseiran, A., Boccardi, F., Braun, V., Kusume, K., Marsch, P., Maternia, M., Queseth, O., Schellmann, M., Schotten, H., & Taoka, H. (2014). Scenarios for 5G Mobile and Wireless Communications: The Vision of the Metis Project. *IEEE Communications Magazine*, Vol. *52*(5), pp. 26-35.

2. Andrews, J. G., Buzzi, S., Choi, W., Hanly, S. V., Lozano, A., Soong, A. C., & Zhang, J. C. (2014). What Will 5G Be? *IEEE Journal on Selected Areas in Communications*, Vol. *32*(6), pp. 1065-1082.

3. IHS. (2016). Connected Devices Internet of Things. Retrieved from https://www.forbes.com/sites/louiscolumbus/2016/11/27/roundup-of-internet-of-things-forecasts-and-market-estimates-2016/#65a53bf292d5.

4. Mahon, S. (2017). The 5G Effect on Rf Filter Technologies. *IEEE Transactions on Semiconductor Manufacturing*, Vol. *30*(4), pp. 494-499.

5. Wi-Fi Channels, Frequencies, Bands & Bandwidths. Retrieved from https://www.electronics-notes.com/articles/connectivity/wifi-ieee-802-11/wi-fi-location-coverage.php.

6. Pensala, T. (2011). *Thin Film Bulk Acoustic Wave Devices: Performance Optimization and Modeling* (1st ed.): VTT Publications, pp. 14 -17.

7. Slobodnik, A. J. (1976). Surface Acoustic Waves and SAW Materials. *Proceedings of the IEEE*, Vol. *64*(5), pp. 581-595.

8. Maines, J., & Paige, E. G. (1976). Surface-Acoustic-Wave Devices for Signal Processing Applications. In *IEEE Proceedings* (Vol. 64, pp. 639-652).

9. Benes, E., Groschl, M., Seifert, F., & Pohl, A. (1998). Comparison between BAW and SAW Sensor Principles. *IEEE Transactions on Ultrasonics, Ferroelectrics, and Frequency Control*, Vol. *45*(5), pp. 1314-1330.

10. Akiyama, M., Kamohara, T., Kano, K., Teshigahara, A., Takeuchi, Y., & Kawahara, N. (2009). Enhancement of Piezoelectric Response in Scandium Aluminum Nitride Alloy Thin Films Prepared by Dual Reactive Cosputtering. *Advanced Materials*, Vol. *21*(5), pp. 593-596.

11. Lueng, C., Chan, H. L., Surya, C., & Choy, C. (2000). Piezoelectric Coefficient of Aluminum Nitride and Gallium Nitride. *Journal of Applied Physics*, Vol. *88*(9), pp. 5360-5363.

12. Corrales López, E., De Paco Sánchez, P., & Menéndez Nadal, Ó. (2011). *Analysis and Design of Bulk Acoustic Wave Filters Based on Acoustically Coupled Resonators.* (Doctoral dissertation), Universitat Autònoma de Barcelona, Retrieved from https://ddd.uab.cat/pub/tesis/2011/hdl_10803_42011/ecl1de1.pdf

13. Herklotz, A., Rus, S. F., & Ward, T. Z. (2016). Continuously Controlled Optical Band Gap in Oxide Semiconductor Thin Films. *Nano Letters*, Vol. *16*(3), pp. 1782-1786.

14. Lorenz, K., Wendler, E., Redondo-Cubero, A., Catarino, N., Chauvat, M.-P., Schwaiger, S., Scholz, F., Alves, E., & Ruterana, P. (2017). Implantation Damage Formation in a-, c- and m-Plane GaN. *Acta Materialia*, Vol. *123*, pp. 177-187.

15. Akiyama, M., Kano, K., & Teshigahara, A. (2009). Influence of Growth Temperature and Scandium Concentration on Piezoelectric Response of Scandium Aluminum Nitride Alloy Thin Films. *Applied Physics Letters*, Vol. *95*(16), pp. 162107.

16. Tasnadi, F., Alling, B., Höglund, C., Wingqvist, G., Birch, J., Hultman, L., & Abrikosov, I. A. (2010). Origin of the Anomalous Piezoelectric Response in Wurtzite Sc X Al 1− X N Alloys. *Physical Review Letters*, Vol. *104*(13), pp. 137601.

17. Zhang, Y., Ram, M. K., Stefanakos, E. K., & Goswami, D. Y. (2012). Synthesis, Characterization, and Applications of ZnO Nanowires. *Journal of Nanomaterials*, Vol. *2012*, pp. 20.

18. Fuentes Iriarte, G. (2003). *AlN Thin Film Electroacoustic Devices.* (Doctoral dissertation), Retrieved from http://www.diva-portal.org/smash/record.jsf?pid=diva2%3A162491&dswid=-7137

19. Tonisch, K., Cimalla, V., Foerster, C., Romanus, H., Ambacher, O., & Dontsov, D. (2006). Piezoelectric Properties of Polycrystalline AlN Thin Films for Mems Application. *Sensors Actuators A: Physical*, Vol. *132*(2), pp. 658-663.

20. Morkoç, H., & Özgür, Ü. (2008). *Zinc Oxide: Fundamentals, Materials and Device Technology*: John Wiley & Sons.

21. Arnau, A., & Soares, D. (2009). Fundamentals of Piezoelectricity. In *Piezoelectric Transducers and Applications* (pp. 1-38): Springer.

22. Dineva, P., Gross, D., Müller, R., & Rangelov, T. (2014). *Dynamic Fracture of Piezoelectric Materials* (1st ed. Vol. 10): Springer.

23. Jesse, S., Mirman, B., & Kalinin, S. V. (2006). Resonance Enhancement in Piezoresponse Force Microscopy: Mapping Electromechanical Activity, Contact Stiffness, and Q Factor. *Applied Physics Letters*, Vol. *89*(2), pp. 022906.

24. Kuball, M. (2001). Raman Spectroscopy of GaN, AlGaN and AlN for Process and Growth Monitoring/Control. *Surface Interface Analysis: An international journal devoted to the development application of techniques for the analysis of surfaces, interfaces, thin films*, Vol. *31*(10), pp. 987-999.

25. Russo, V., Ghidelli, M., Gondoni, P., Casari, C. S., & Li Bassi, A. (2014). Multi-Wavelength Raman Scattering of Nanostructured Al-Doped Zinc Oxide. *Journal of Applied Physics*, Vol. *115*(7), pp. 073508.

26. Prokofyeva, T., Seon, M., Vanbuskirk, J., Holtz, M., Nikishin, S., Faleev, N., Temkin, H., & Zollner, S. (2001). Vibrational Properties of AlN Grown on (111)-Oriented Silicon. *Physical Review B*, Vol. *63*(12), pp. 125313.

27. Meng, W., Sell, J., Perry, T., Rehn, L., & Baldo, P. (1994). Growth of Aluminum Nitride Thin Films on Si (111) and Si (001): Structural Characteristics and Development of Intrinsic Stresses. *Journal of Applied Physics*, Vol. *75*(7), pp. 3446-3455.

28. McNeil, L. E., Grimsditch, M., & French, R. H. (1993). Vibrational Spectroscopy of Aluminum Nitride. *Journal of the American Ceramic Society*, Vol. *76*(5), pp. 1132-1136.

29. Semond, F., Cordier, Y., Grandjean, N., Natali, F., Damilano, B., Vézian, S., & Massies, J. (2001). Molecular Beam Epitaxy of Group-III Nitrides on Silicon Substrates: Growth, Properties and Device Applications. *Physica Status Solidi (a)*, Vol. *188*(2), pp. 501-510.

30. Le Louarn, A., Vézian, S., Semond, F., & Massies, J. (2009). AlN Buffer Layer Growth for GaN Epitaxy on (1 1 1) Si: Al or N First? *Journal of Crystal Growth*, Vol. *311*(12), pp. 3278-3284.

31. Leveneur, J. (2013). *Ion Beam Synthesis and Properties of Magnetic Nanoparticles in Sio2.* (Doctoral dissertation, ResearchSpace@ Auckland),

32. Nastasi, M., Michael, N., Mayer, J., Hirvonen, J. K., & James, M. (1996). *Ion-Solid Interactions: Fundamentals and Applications*: Cambridge University Press.

33. Hubler, G. K. (1987). Ion Beam Processing. *Research Gate*. Retrieved from https://www.researchgate.net/publication/322725607.

34. Ziegler, J. F., & Biersack, J. P. (2008). *SRIM-2008, Stopping Power and Range of Ions in Matter*.

35. Ziegler, J. F., & Biersack, J. P. (1985). The Stopping and Range of Ions in Matter. In *Treatise on Heavy-Ion Science* (pp. 93-129): Springer.

36. Ziegler, J. F., Ziegler, M. D., & Biersack, J. P. (2010). SRIM –the Stopping and Range of Ions in Matter (2010). *Nuclear Instruments Methods in Physics Research Section B: Beam Interactions with Materials and Atoms*, Vol. *268*(11-12), pp. 1818-1823.

37. Ferraro, J. R. (2003). *Introductory Raman Spectroscopy*: Elsevier.

38. Long, D. A. (2002). *The Raman Effect* (1st ed.): Wiley.

39. Bradley, M. (2007). Curve Fitting in Raman and IR Spectroscopy: Basic Theory of Line Shapes and Applications. *Thermo Fisher Scientific*, Vol. *50733*.

40. Gouadec, G., & Colomban, P. (2007). Raman Spectroscopy of Nanomaterials: How Spectra Relate to Disorder, Particle Size and Mechanical Properties. *Progress in Crystal Growth and Characterization of Materials*, Vol. *53*(1), pp. 1-56.

41. Mante, N., Rennesson, S., Frayssinet, E., Largeau, L., Semond, F., Rouviere, J.-L., Feuillet, G., & Vennéguès, P. (2018). Proposition of a Model Elucidating the AlN-on-Si (111) Microstructure. *Journal of Applied Physics*, Vol. *123*(21), pp. 215701.

42. Kosacki, I., Suzuki, T., Anderson, H. U., & Colomban, P. (2002). Raman Scattering and Lattice Defects in Nanocrystalline Ceo2 Thin Films. *Solid State Ionics*, Vol. *149*(1-2), pp. 99-105.

43. Parayanthal, P., & Pollak, F. H. (1984). Raman Scattering in Alloy Semiconductors:" Spatial Correlation" Model. *Physical Review Letters*, Vol. *52*(20), pp. 1822.

44. Ermrich, M., & Opper, D. (2013). *XRD for the Analyst* (2nd ed.): PANalytical

45. Baskaran, S. (2010). *Structure and Regulation of Yeast Glycogen Synthase*. (Doctoral dissertation), Retrieved from https://scholarworks.iupui.edu/handle/1805/2278

46. Lübben, J. F. (2007). *Atomic Force Microscopy on Fibers*. Retrieved from https://pdfs.semanticscholar.org/ba83/701cb66007a9a18432d0d0f7fcb8ac0744f4.pdf

47. Cordier, Y., Comyn, R., Frayssinet, E., Khoury, M., Lesecq, M., Defrance, N., & De Jaeger, J. C. (2018). Influence of AlN Growth Temperature on the Electrical Properties of Buffer Layers for GaN Hemts on Silicon. *Physica Status Solidi (a)*, Vol. *215*(9), pp. 1700637.

48. Frayssinet, E., Leclaire, P., Mohdad, J., Latrach, S., Chenot, S., Nemoz, M., Damilano, B., & Cordier, Y. (2017). Influence of Metal-Organic Vapor Phase Epitaxy Parameters and Si (111) Substrate Type on the Properties of AlGaN/GaN Hemts with Thin Simple Buffer. *Physica Status Solidi (a)*, Vol. *214*(4), pp. 1600419.

49. Zhang, M., Yang, J., Si, C., Han, G., Zhao, Y., & Ning, J. (2015). Research on the Piezoelectric Properties of AlN Thin Films for Mems Applications. *Micromachines*, Vol. *6*(9), pp. 1236-1248.

50. Morito, K., Iwazaki, Y., Suzuki, T., & Fujimoto, M. (2003). Electric Field Induced Piezoelectric Resonance in the Micrometer to Millimeter Waveband in a Thin Film Srtio 3 Capacitor. *Journal of Applied Physics*, Vol. *94*(8), pp. 5199-5205.

51.   Ching, W., & Harmon, B. (1986). Electronic Structure of AlN. *Physical Review B*, Vol. *34*(8), pp. 5305.

52.   Schulz, H., & Thiemann, K. (1977). Crystal Structure Refinement of AlN and GaN. *Solid State Communications*, Vol. *23*(11), pp. 815-819.

53.   Faye, D. N., Wendler, E., Felizardo, M., Magalhães, S., Alves, E., Brunner, F., Weyers, M., & Lorenz, K. (2016). Mechanisms of Implantation Damage Formation in Al X Ga1–X N Compounds. *The Journal of Physical Chemistry C*, Vol. *120*(13), pp. 7277-7283.

54.   Uchinokura, K., Sekine, T., & Matsuura, E. (1972). Raman Scattering by Silicon. *Solid State Communications*, Vol. *11*(1), pp. 47-49.

55.   Kuball, M., Hayes, J., Prins, A., Van Uden, N., Dunstan, D., Shi, Y., & Edgar, J. H. (2001). Raman Scattering Studies on Single-Crystalline Bulk AlN under High Pressures. *Applied Physics Letters*, Vol. *78*(6), pp. 724-726.

56.   Rodriguez, B., Kim, D., Kingon, A., & Nemanich, R. (2001). Measurement of the Effective Piezoelectric Constant of Nitride Thin Films and Heterostructures Using Scanning Force Microscopy. *MRS Proceedings*, Vol. *693*. doi:10.1557/PROC-693-I9.9.1

57.   Kudriavtsev, Y., Villegas, A., Godines, A., & Asomoza, R. (2005). Calculation of the Surface Binding Energy for Ion Sputtered Particles. *Applied Surface Science*, Vol. *239*(3-4), pp. 273-278.

58.   Murmu, P. P., Kennedy, J. V., Markwitz, A., & Ruck, B. J. (2009). Compositional and Structural Study of Gd Implanted ZnO Films. In *AIP Conference Proceedings* (Vol. 1151, pp. 185-188): AIP.

59.   Palmetshofer, L. (2011). Rutherford Back-Scattering Spectroscopy (RBS). *Surface and Thin Film Analysis: A Compendium of Principles, Instrumentation, and Applications*, pp. 191-202.

60.   Williams, G. V., Kennedy, J., Murmu, P. P., & Rubanov, S. (2018). Structural and Magnetic Properties of near Surface Superparamagnetic Ni1-Xfex Nanoparticles in Sio2 Formed by Low Energy Dual Ion Implantation with Different Fluences. *Applied Surface Science*, Vol. *449*, pp. 399-404.

61.   Yang, J.-c., Meng, X.-q., Yang, C.-t., & Zhang, Y. (2013). Influence of Sputtering Power on Crystal Quality and Electrical Properties of Sc-Doped AlN Film Prepared by Dc Magnetron Sputtering. *Applied Surface Science*, Vol. *287*, pp. 355-358.

62.   Zhang, Y., Zhu, W., Zhou, D., Yang, Y., & Yang, C. (2015). Effects of Sputtering Atmosphere on the Properties of C-Plane Scaln Thin Films Prepared on Sapphire Substrate. *Journal of Materials Science: Materials in Electronics*, Vol. *26*(1), pp. 472-478.